

THESIS

A PERSONAL, THERMOPHORETIC SAMPLER FOR AIRBORNE NANOPARTICLES

Submitted by

Daniel Lee Thayer

Department of Mechanical Engineering

In partial fulfillment of the requirements

For the Degree of Master of Science

Colorado State University

Fort Collins, Colorado

Summer 2010

COLORADO STATE UNIVERSITY

May 21, 2010

WE HEREBY RECOMMEND THAT THE THESIS PREPARED UNDER OUR SUPERVISION BY DANIEL LEE THAYER ENTITLED A PERSONAL, THERMOPHORETIC SAMPLER FOR AIRBORNE NANOPARTICLES, BE ACCEPTED AS FULFILLING IN PART REQUIREMENTS FOR THE DEGREE OF MASTER OF SCIENCE.

Committee on Graduate Work



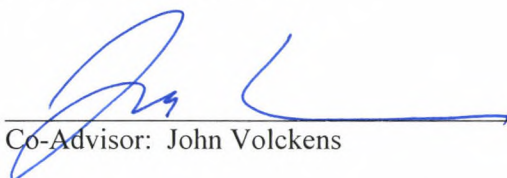
Ketul Popat



Amy Prieto



Advisor: Anthony Marchese



Co-Advisor: John Volckens



Department Head: Allan Kirkpatrick

ABSTRACT OF THESIS

A PERSONAL, THERMOPHORETIC SAMPLER FOR AIRBORNE NANOPARTICLES

Engineered nanoparticles are materials with at least one dimension measuring less than 100 nm that are designed on the molecular scale to produce unique or enhanced properties that differ from the bulk material. However, the same properties that make engineered nanoparticles attractive to industry also may present potential health risks to the workers who manufacture them. Very little human exposure data exist for these particles, although they are known enter the body through a number of routes (e.g., respiration, dermal penetrations, and ingestion). Nanoparticles that enter the body can also translocate from one organ to another by virtue of their small size. A cost-effective personal sampler is necessary to evaluate levels of worker exposure to these materials to determine the relative levels of individual risk. Such a sampler must be capable of collecting nanoparticles with high efficiency for subsequent analysis of size, surface chemistry, morphology, and other properties. In addition, the sampler must be able to differentiate between *incidental* nanoparticles, which are nanoparticles that are naturally present in the environment, and *engineered* nanoparticles. As detailed in this thesis, a small thermal precipitator was designed to measure breathing-zone concentrations of airborne nanoparticles. The thermal precipitator samples aerosol by producing a $1000\text{ }^{\circ}\text{C}\cdot\text{cm}^{-1}$ temperature gradient between two aluminum plates (0.1 cm separation distance) using a resistive heater, a thermoelectric cooler, a temperature controller, and two thermistor sensors. The collection

efficiency was evaluated for 15, 51, 100, and 240 nm particles at flow rates of 5 and 20 mL/min. Tests were also performed with a zero temperature gradient to determine losses in the device for measurement correction. The homogeneity of particle collection across the collection surface was evaluated using electron microscopy and imaging software. The results indicate that thermal precipitation is a feasible approach for personal monitoring of airborne nanoparticle concentrations in the workplace.

Daniel Lee Thayer
Department of Mechanical Engineering
Colorado State University
Fort Collins, CO 80523
Summer 2010

Table of Contents

List of Figures	vii
List of Tables.....	ix
1 Introduction.....	1
1.1 Background.....	1
1.2 Current Measurement Capabilities	4
1.3 Previous Work	7
1.4 Theory for Thermophoretic Particle Collection	9
1.5 Problem Statement: Improvements of a Thermophoretic Sampler Prototype.....	11
2 Methods and Materials.....	15
2.1 Thermophoretic Sampler Design.....	15
2.2 Device Calculations.....	18
2.3 Experimental Setup	22
2.3.1 Collection Efficiency: 5 mL/min and 20 mL/min Flow.....	22
2.3.2 Diffusion Loss Tests: 6.7 mL/min Flow	26
2.3.3 Collection Uniformity Tests.....	27
3 Results.....	30
3.1 Collection Efficiency: Device On, 5 mL/min Flow	30
3.2 Collection Efficiency: Device On, 20 mL/min Flow	31
3.3 Diffusion Loss Tests: 6.7 mL/min Flow.....	32
3.4 Collection Uniformity Tests.....	32
4 Discussion of Results	35
4.1 Collection Efficiency: Device On.....	35
4.2 Diffusion Loss Tests: 6.7 mL/min Flow.....	37
4.3 Collection Uniformity Tests	39
5 Conclusions and Suggestions for Future Research	41
References	44
Appendix A – Particle Adhesion Calculations.....	46
Appendix B – Thermophoretic Sampler Design Calculations (Equation Set 1).....	47
Appendix C – Thermophoretic Sampler Design Calculations (Equation Set 2).....	52

Appendix D – ImageJ Particle Counting Procedure 60

List of Figures

Figure 1. Illustration of the principle of thermophoresis.

Figure 2. Three-dimensional model and photograph of the 2009 Colorado State University Senior Design Team thermophoretic sampler prototype.

Figure 3. Fluent computer simulation of particle transport within the Senior Design Team prototype showing aerosol dispersion within the collection zone.

Figure 4. Three-dimensional model and photograph of the new thermophoretic sampler prototype.

Figure 5. Photograph of the thermophoretic sampler as typically worn on a human torso.

Figure 6. Three-dimensional model of the particle collection plate with magnet and O-ring seal.

Figure 7. Model parameters used to calculate the particle collection distance.

Figure 8. Estimated particle diffusion losses for the (6.35 mm ID, 635 mm long) sample lines and the thermophoretic sampler.

Figure 9. Experimental setup of the collection efficiency tests.

Figure 10. Experimental setup of the collection uniformity tests.

Figure 11. SEM imaging locations on the particle collection surface.

Figure 12. Measured collection efficiencies as a function of particle size and flow rate.

Figure 13. Uniformity of particle deposition across the collection surface as a function of particle size.

Figure 14. Example SEM images from the centerline of the particle collection plate.

A) Near the front of the plate. B) At the center of the plate. C) Near the end of the plate.

List of Tables

Table 1. Experimental Conditions for Particle Collection Efficiency Tests with an Applied Temperature Gradient.

Table 2. Experimental Conditions for Particle Collection Efficiency Tests without an Applied Temperature Gradient.

Table 3. Experimental Conditions for Collection Uniformity Tests.

Table 4. Tukey's HSD multiple comparison test for log transformed 6.7 mL/min data.

1 Introduction

1.1 Background

Engineered nanoparticles are materials designed on the molecular scale with at least one dimension measuring less than 100 nm. These particles often possess material properties that are enhanced due to their small size. For example, one property that affects the catalytic activity of a material is surface area. The ratio of surface area to mass of a material increases with decreasing particle size, allowing new materials to be used in applications previously thought impractical. As the nanotechnology industry develops, the use of engineered nanoparticles is expected to increase dramatically (Tsuji *et al.*, 2005, Nkwenti *et al.*, 2009, Gonzalez *et al.*, 2005). Some applications of these materials include miniature electronics (e.g. high efficiency wires or semiconductors), compact computer memory, high strength/light-weight construction materials, miniature electromechanical systems, and photovoltaic and energy storage devices (Tsuji *et al.*, 2005, Arico *et al.*, 2005). Hundreds of companies in the United States already incorporate nanomaterials into a wide variety of manufactured products (Thomas *et al.*, 2006). For example, nano-structured materials in lithium-ion batteries may revolutionize the energy industry by increasing storage capacity and cycle-life (Arico *et al.*, 2005, Chan *et al.*, 2007). Nanotechnologies also possess the potential for breakthrough discoveries in the area of drug delivery (Dames *et al.*, 2009, Oberdorster *et al.*, 2005, Jong and Borm, 2008). A recent study demonstrated experimentally and by computer simulation that magnetic aerosol droplets could be used for targeted drug delivery in the lungs. This technique may be useful for treating localized lung diseases, such as cancer (Dames *et al.*, 2009).

As these new nanotechnologies develop, there is a growing concern about the adverse health effects that engineered nanoparticles may pose to both humans and the environment (Maynard *et al.*, 2006, Weisner *et al.*, 2009). Unfortunately, the same unique properties that make nanoparticles so desirable also make them potentially dangerous (Thomas *et al.*, 2006, Maynard *et al.*, 2006). For example, the high surface area of nanoparticle catalysts also makes them more reactive in biological systems (Tsuji *et al.*, 2005). Although there are many possible routes for nanoparticles to enter the body (e.g., dermal penetration and ingestion), exposure assessment for multiple pathways is incredibly difficult and complex. This thesis focuses only on monitoring engineered nanoparticles entering the body via inhalation.

Nanoparticles of various sizes deposit effectively in all three parts of the respiratory system. For instance, 1 nm particles deposit with 90% collection efficiency in the nasopharyngeal region, while only depositing with 10% efficiency in the tracheobronchial region and virtually no deposition in the alveolar region. Conversely, 5 nm particles deposit with roughly 30% collection efficiency in all three regions. Particles with a diameter of 20 nm deposit with approximately 50% collection efficiency in the alveolar region and about 15% in each of the other two regions (Oberdorster *et al.*, 2005).

The small size of nanoparticles enables them to cross barriers in the respiratory system once they deposit. This biological mobility can be exploited for medical imaging and therapeutic procedures, but will also occur for other nanomaterials that are unintentionally released and inhaled. A percentage of these inhaled particles will likely be transported along the mucociliary escalator (the pathway formed by the mucous-coated cilia in the tracheobronchial region) and swallowed into the gastrointestinal tract. Particles entering the gastrointestinal tract in this way have been shown to be eliminated quickly (Oberdorster *et al.*, 2005). However, translocation of these particles to other organ systems may be more harmful. For example, particles could enter the circulatory system by diffusion through the alveolar cell walls. Once in the circulatory system, they would be transported to the heart or other organ systems (Tsuji *et al.*, 2005, Thomas

et al., 2006, Oberdorster *et al.*, 2005, Schulte *et al.*, 2009, Fissan *et al.*, 2007, Furuuchi *et al.*, 2010). The liver is the main distribution site for Kupffer cells (specialized macrophages), which will likely phagocytize nanoparticles that enter the body (Oberdorster *et al.*, 2005). Hence, particles entering the circulatory system may be deposited in the liver in higher concentrations than other organs. Another concern is that nanoparticles may be able to reach the brain directly via olfactory and trigeminal nerve axons (Oberdorster *et al.*, 2005).

Previous studies have shown associations between nanoparticles and inflammatory responses that resulted in morbidity and mortality in more susceptible populations (Maynard and Kuempel, 2005). Recent studies suggest that nanometer-sized particles may cause a higher inflammatory response per given mass than larger, sub-micrometer sized particles (Tsuji *et al.*, 2005). This high sensitivity to low concentrations is important since the nanomaterials may be present at trace levels in air (Weisner *et al.*, 2009). For example, polytetrafluoroethylene (PTFE) fumes have been shown to be highly toxic to birds and mammals. However, a study showed that PTFE particles that were allowed to age slightly (aggregating into larger agglomerates > 100 nm) were far less toxic (Oberdorster *et al.*, 2005). Tsuji *et al.* (2005) reported that TiO₂ nanoparticles (~25 nm) produced equivalent numbers of lung tumors in rats at less than one tenth the inhaled exposure mass concentrations of fine-sized TiO₂ particles (~300 nm). However, debate continues on whether particle size is the dominant factor in determining toxicity. Nanoparticles vary in size, shape, composition, charge, crystallinity, solubility, and impurities, with each factor leading to different potential toxicities (Schulte *et al.*, 2009). In addition, engineered nanoparticles are typically monodisperse, as opposed to the polydisperse nanoparticles naturally present in the environment, which may also lead to higher toxicity (Oberdorster *et al.*, 2005).

Pre-emptive regulation to protect workers in facilities that manufacture and process nanomaterials threatens to slow down research and make new projects less desirable to investors (Monica *et al.*, 2007). More information concerning the toxicological properties of nanoparticles is necessary to make informed decisions to encourage their safe development. However, current

studies often lack adequate measurement capabilities for the collection and characterization of nanoparticles.

1.2 Current Measurement Capabilities

To evaluate the potential health effects resulting from exposure to airborne nanoparticles, a method to measure exposure levels must be determined. However, the particle property or properties that most affect toxicity remain unknown. Therefore, the capability to measure multiple particle characteristics is necessary (Tsuji *et al.*, 2006, Thomas *et al.*, 2006, Maynard *et al.*, 2006, Handy *et al.* 2005, Peters *et al.*, 2009, Fujitani and Kobayashi, 2008, and Weisner *et al.*, 2009). Current measurement instruments are often too expensive or insufficiently sensitive for use in studies involving human exposure to engineered nanoparticles (Tsuji *et al.*, 2005, Thomas *et al.*, 2006, Handy *et al.*, 2006, Fujitani and Kobayashi, 2008). These measurements generally rely on mass concentrations or surface properties of bulk materials, which may not be appropriate metrics for characterizing an inhalation risk. In addition, nanoparticles are generally present in concentrations too small for mass measurement, which is often used to determine the amount of material to which a worker is exposed. Particle number concentration or size distributions are likely to be much better metrics because of the information that can be inferred (e.g. surface area and mass).

A number of studies have used scanning electron microscopy (SEM) and transmission electron microscopy (TEM) to image particles collected on a variety of substrates (Handy *et al.*, 2005, Peters *et al.*, 2009, Fujitani *et al.*, 2008, Han *et al.*, 2008, Fujitani and Kobayashi, 2008, Nkwenti *et al.*, 2009, Gonzalez *et al.*, 2005). In these studies, the SEM and TEM images were used to determine projected surface area, size, and other morphological characteristics. The disadvantage of these instruments is that they require samples to be collected and stored for analysis at a later time. Moreover, the data collection process (e.g. imaging particles for counting and sizing) can be very time consuming (Handy *et al.*, 2006 Fujitani *et al.*, 2008, Han *et al.*, 2008,

Schulte *et al.*, 2009, Peters *et al.*, 2009, Fujitani and Kobayashi, 2008, Nkwenti *et al.*, 2009). Several types of optical measurement devices are commonly used to monitor nanoparticle concentrations, size distributions, and other important aerosol properties. Aerodynamic particle sizers (APS) and optical particle counters can measure aerosol size distributions (aerodynamic diameter) directly. Both of these devices are limited to measuring particles larger than about 300 nm (Fujitani and Kobayashi, 2008). Particles below this size are too small to scatter sufficient light for detection, unless their concentration is very high, such as with photon correlation spectroscopy. Photon correlation spectroscopy instruments measure fluctuations in light scattered by a particle's Brownian motion when suspended in liquid. The scattered light is monitored on the order of milliseconds or microseconds and depends on the amount of constructive and destructive interference at the moment of measurement. Brownian motion is dependent only on particle size, and so the instrument is able to determine the size distribution of the hydrosol from the pattern of scattered light. However, the fluctuations in scattered light must be greater than the noise of the system (such as temperature fluctuations and the inherent electrical noise of the instrument). Photon correlation spectroscopy requires high concentrations of nanoparticles in solution, which precludes the use of this technique for measurements in air. Condensation particle counters use a supersaturated airstream to grow small particles until they are large enough to be detected by light scattering. However, condensation particle counters cannot differentiate between particles of different sizes. To avoid these limitations, multiple instruments are often used in conjunction in nanoparticle exposure studies (Handy *et al.*, 2006, Fujitani *et al.*, 2008, Han *et al.*, 2008, Schulte *et al.*, 2009, Peters *et al.*, 2009, Fujitani and Kobayashi, 2008, Nkwenti *et al.*, 2009). A sequential mobility particle sizer combines a differential mobility analyzer, which selects airborne particles of a given electrical mobility, which is related to particle size, along with a condensation particle counter to measure particle number concentration within a selected size range. However, this technique cannot provide information about particle shape and

chemical composition and such an instrument is too large for *personal* monitoring of nanoparticle concentrations within an individual's breathing-zone.

To manage the possible risks associated with engineered nanoparticles, a universal sampler is urgently needed, particularly for the safety of workers involved in designing and manufacturing engineered nanomaterials (Weisner *et al.*, 2009). Since these workers may be exposed to many types of nanoparticles at high concentrations, an instrument that only measures one particle property will likely be insufficient. Therefore, the objective of the present work is to develop a personal sampler for airborne nanoparticles, allowing for the measurement of nanoparticle concentrations within the breathing-zone of an exposed worker. Additionally, the device should be capable of differentiating between incidental and engineered nanoparticles in a given sample of air. None of the aforementioned instruments are portable and are therefore not suitable for use as personal samplers, which must be small, lightweight, and portable. Ideally, a personal sampler would also be sufficiently inexpensive to facilitate widespread use (Maynard *et al.*, 2006).

Many existing instruments show promise for measuring very specific properties of nanoparticles. Isothermal adsorption has been used for decades to measure the surface area of powders, but it is unclear how effective this method would be for the low concentrations involved with nanoparticles (Tsuji *et al.*, 2005). Diffusion charging instruments have been tested as plausible surface area measurement instruments with some success, but are currently too large to be used as personal samplers. One such instrument of particular interest was modified from a TSI Inc. electrical aerosol detector to measure the surface area of particles deposited in specific areas of the respiratory system (Fissan *et al.*, 2007). Several other portable devices exist that can be used for very specific nanomaterial measurements. For example, a portable aethalometer was used to measure carbon black levels in a study monitoring worker exposure in a multiwalled carbon nanotube factory (Han *et al.*, 2008). Although these instruments are useful for monitoring certain properties of airborne nanoparticles, a more universal sampler is needed, since it is not yet clear which properties are most closely linked to toxicity. Unexpected interactions between

several properties may also be important in determining the toxicity of nanomaterials (Tsuji *et al.*, 2005). For example, size may influence which barriers in the body nanoparticles can cross, but actual health effects of the nanoparticles could be determined by surface charge, chemical composition, or particle shape (Jong and Borm, 2008). Though no effective personal, nanoparticle samplers are available commercially, several prototype samplers have been tested. Some of these prototypes may be adapted for use as personal samplers.

1.3 Previous Work

Of the many personal samplers developed and tested, three devices that show potential for use in monitoring worker exposures are described below. The first of these prototypes used an ‘inertial filter’ to sample particles from within an individual’s breathing zone (Furuuchi *et al.*, 2010). The device was tested for 6-8 hour sampling periods, which corresponded to a typical work shift. Unlike the systems described in the previous section, the filters employed by Furuuchi *et al.* (2010) do have a nano-size cutoff diameter under a moderate pressure drop. The Furuuchi device can also be operated at a sufficiently high flow rate to collect particle concentrations adequate for analysis in a relatively short time. The pressure drop due to filter loading was also determined to be acceptable for reliable pump operation. However, the size cutoff point for this device was approximately 140 nm, which is outside the nanoparticle range of interest. This cutoff point would have to be decreased substantially for use as a nanoparticle sampler, which may not be feasible with inertial filters.

The second and third studies used thermophoresis (which will be described in detail in the following section) to collect nanoparticles. In these studies, electron microscopy substrates were used as the particle collection surface to facilitate subsequent particle analysis (Nkwenti *et al.*, 2009, Gonzalez *et al.*, 2005). Earlier thermophoretic sampler designs used a resistive wire as the heat source for the temperature gradient. However, the wire created a non-uniform temperature field, which led to non-uniform particle collection (Gonzalez *et al.*, 2005). The earlier studies by

Gonzalez *et al.* (2005) and Nkwenti *et al.* (2009) suggested that if the particles have a homogeneous spatial distribution on the collection substrate, fewer electron microscope images are necessary to obtain an accurate representation of the sample. Representative imaging is important, since these images are used to reconstruct the concentration and size distribution of the sampled aerosol.

The thermophoretic precipitator described by Gonzalez *et al.* (2005) collected particles on an aluminum foil substrate, which was analyzed using SEM to verify that the collection was homogeneous. Samples were also collected onto TEM grids (and subsequently imaged by TEM) to determine the uniformity of deposition using a different substrate. Computational fluid dynamics models were constructed to determine the uniformity of flow rate and temperature gradient in the device (Gonzalez *et al.*, 2005). These computer simulations included the effects of diffusion losses and non-uniform temperature gradients. This study also compared the collection efficiencies predicted by computer simulation to those predicted by analytical models for flow rates from 10 to 100 mL/min values. Their results suggest that particle collection was uniform and near 100% at flow rates below 15 mL/min. Collection efficiency decreased dramatically as the flow rate was increased beyond 15 mL/min. This prototype, while small and effective as a nanoparticle sampler, was not portable since it used cold tap water to control the temperature of the collection surface (Gonzalez *et al.*, 2005).

A more recent study by Nkwenti *et al.* (2009) describes calculations for the collection efficiency of a prototype personal, thermophoretic sampler. The calculations were compared to computer simulations modeling the flow and temperature gradient within the device. Simulations were performed with the device in various orientations to determine the effect of gravity on collection efficiency, which showed no significant effect. The simulation was repeated for particle sizes ranging from 20 – 1000 nm of standard density ($\rho = 1.0 \text{ g/cm}^3$) and 7.9 g/cm³ (density of iron) at a flow rate of 2 mL/min. The results suggested that the design would perform well for sizes up to 300 nm and deposition would be sufficiently uniform along the collection substrate at

a sample flow rate of 2 mL/min. A steady, 2 mL/min flow rate can be difficult to maintain, though Nkwenti *et al.* (2005) did not address this issue. A prototype of this design has been built and is currently being tested for agreement against the model simulations (Nkwenti *et al.*, 2009).

These studies demonstrate that thermophoresis can be applied in the design of airborne nanoparticle samplers. However, the devices studied to date were not operated in environments that contained incidental aerosols. The capability to differentiate between *incidental* and *engineered* nanoparticles in air is very important. Incidental nanoparticles can be formed by natural processes (such as natural fullerenes formed during volcanic activity and forest fires) (Oberdorster *et al.*, 2005), biogenic processes (such as ferritin, an iron storage protein about 12 nm in diameter) (Oberdorster *et al.*, 2005), or anthropogenic (such as diesel engine exhaust) (Fujitani *et al.*, 2008). Since the nanoparticles are collected onto electron microscopy substrates, particle size and morphology can be used to differentiate some engineered nanoparticles from incidental nanoparticles. This process can be facilitated with the use of imaging software. Chemical analysis of the particles is also possible without transferring the samples to different substrates, as energy dispersive techniques can be used in parallel with electron microscopy.

1.4 Theory for Thermophoretic Particle Collection

Thermophoretic aerosol collectors use a temperature gradient to impart a thermophoretic force on particles, causing them to migrate toward a collection surface. The temperature gradient is created within a narrow flow channel, wherein one surface is heated and the other surface is cooled. A diagram of the flow channel is presented in Figure 1 (not to scale).

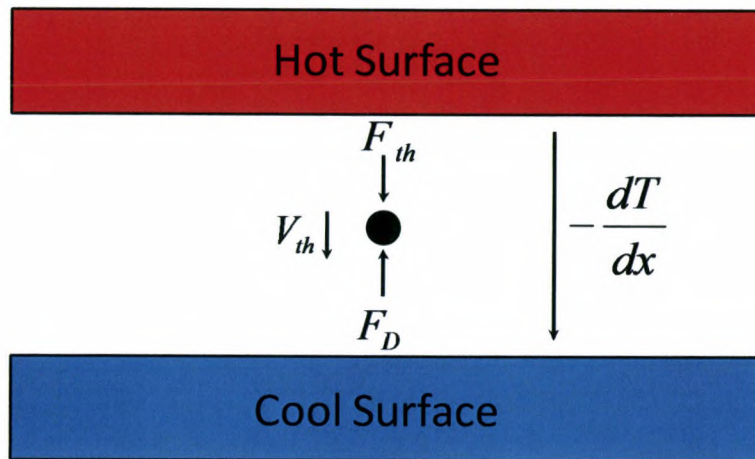


Figure 1. Illustration of the principle of thermophoresis.

In many aerosol applications, thermophoretic forces are negligible in comparison to other forces acting on the particles, such as the force due to gravity, or electrostatic forces acting on charged particles. However, when the hot and cold sources are separated by very short distances, a very large temperature gradient can be created, which results in a significant force applied to airborne particles. Aerosol flows into the narrow channel bounded by the hot and cold surfaces. The thermophoretic force is a result of the sum of the momentum transferred from the gas molecules colliding with the suspended particles in the channel. The higher average kinetic energy of the warmer gas molecules results in a net thermophoretic force on the particles in the direction of decreasing temperature gradient. The thermophoretic velocity (V_{th}) is the product of the thermophoretic force (F_{th}) resisted by the Stokes drag force (F_D). The force due to gravity is negligible compared to thermophoretic and drag forces for nanoparticles.

When the particles reach the cold surface, they deposit, due to strong adhesive forces. These adhesive forces vary with particle size, morphology, and the surface characteristics of both the particles and the collection plate. Adhesive forces are generally much greater than other forces that motivate suspended particles, such as those discussed above. Calculations comparing the adhesive forces of the largest and test aerosol diameters to the force due to gravity are found

in Appendix A. For these reasons, thermophoresis represents a simple, but effective technique for aerosol sampling.

Thermophoretic samplers have several advantages. One important advantage is the simplicity of the components needed for operation. A temperature gradient is easy to create and maintain, which increases the feasibility of the design of a small, personal sampler. The operation of a thermophoretic sampler also requires fewer electronic components and computational power in comparison to existing measurement devices such as condensation particle counters and light scattering instruments. The use of an electron microscopy substrate as the collection surface eliminates losses resulting from transferring collected particles from sampler to a substrate, which is necessary for many other types of aerosol samplers.

1.5 Problem Statement: Improvements of a Thermophoretic Sampler Prototype

In 2009, a prototype thermophoretic personal sampler was designed, built, and tested by a team of mechanical engineering students at Colorado State University as their senior design project. The device was designed to collect airborne nanoparticles onto eight TEM grids over an eight hour work shift. Sampled aerosol was directed over each individual grid by rotating the flow exit in a semi-circular path about the collection chamber. The grids were mounted on magnets placed in a cooled aluminum plate, and the flow path was rotated across a new grid each hour. The TEM grids could then be removed for analysis to determine morphology, chemical makeup, and concentration. A 3D model and photograph of this prototype device is presented in Figure 2.

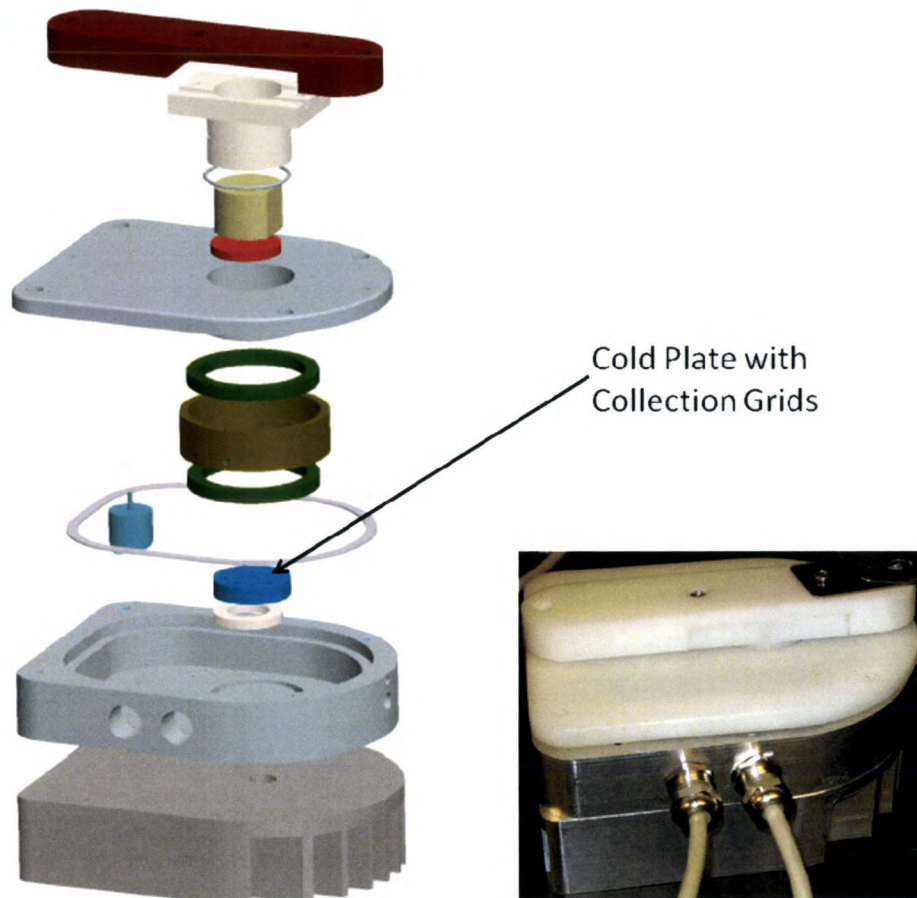


Figure 2. Three-dimensional model and photograph of the 2009 Colorado State University Senior Design Team thermophoretic sampler prototype.

The initial prototype had several serious drawbacks. The device was too large and cumbersome to be acceptable for personal use. The thermophoretic sampler measured approximately 12.7 by 10.2 by 7.5 cm and weighed 901.4 g. The controller, batteries, and pump occupied a large volume and were contained in a backpack, separate from the thermophoretic sampler. The electrical circuitry was not optimized as the system required three separate batteries to supply power to the thermoelectric cooler, heater, and controller. Lead-acid batteries were used, which are relatively inexpensive, but very heavy, weighing a total of 2.6 kg. In addition, the device had large power requirements and therefore large batteries with the capacity to operate

for 6-8 hours (a typical work shift) were necessary. Ideally, the sampler should be powered with a single, lightweight battery.

A fluid flow simulation of this device using FLUENT modeling software (Ansys, Inc., Ann Arbor, Michigan) also revealed problems with contamination within the sample collection zone. A particle track simulation of the sample collection zone is shown in Figure 3. This simulation shows the paths of particles colored as a function of time in the collection chamber. The two large circles represent the hot and cold plates (top and bottom, respectively). The two small circles represent the inlet to the sampler and the small rectangle represents the outlet. The particles cross multiple collection surfaces (these collection surfaces are not shown in Figure 3; see Figure 2), which would give misleading results during subsequent TEM analysis of the grids.

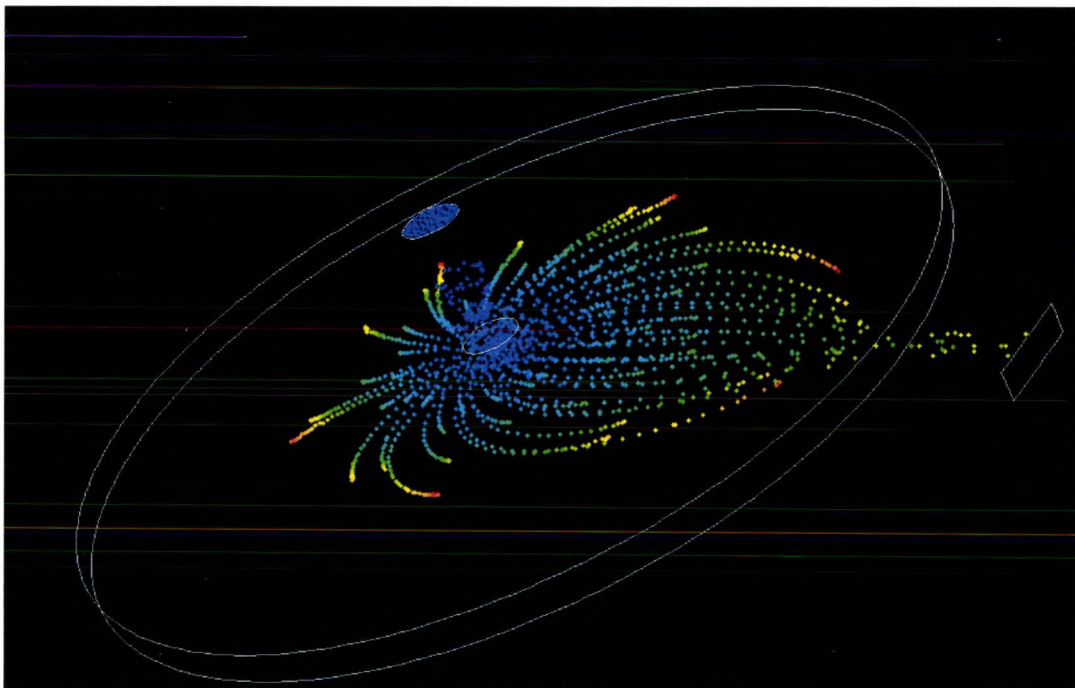


Figure 3. Fluent computer simulation of particle transport within the Senior Design Team prototype showing aerosol dispersion within the collection zone.

Leak tests also revealed that the device did not seal upon application of a vacuum. A pneumatically-sealed collection chamber is essential to prevent contamination and unwanted airflow during instrument operation and handling.

To address these issues, a new, simpler device was designed and tested. This new device, which will be described in Chapter 2, is the subject of this thesis. The new sampler is smaller and lighter than the original design. Because of reduced power needs, it requires only a single, lightweight battery to power all of its electrical systems. The new prototype uses only a single collection plate. However, in future studies, this prototype can be adapted to hold multiple collection plates for time-resolved sampling.

The new prototype has been tested to verify the performance of several characteristics that are critical for reliable, personal thermophoretic sampling. The collection efficiency of the device was measured using a range of particle sizes and at two different flow rates. Diffusion losses within the prototype were determined so that correction factors could be developed to account for particle losses during sampling. Finally, since the distribution of particles collected in the sampler must be homogenous over an area large enough for electron microscopy analysis, the relative flux of particles to the collection surfaces was evaluated using SEM.

2 Methods and Materials

2.1 Thermophoretic Sampler Design

The objective of this work was to develop a personal sampler for airborne nanoparticles. A personal thermophoretic sampling device such as this would be worn within a human's breathing-zone, which implies that the device must be both small and lightweight. Power demands also should be kept at a minimum, so that the sampler can be powered with a small, relatively inexpensive battery. To achieve this objective, a new personal thermophoretic sampler was designed, built, and tested. Figure 4 shows a 3D solid model of the new device, along with a photograph of the fully functioning prototype.

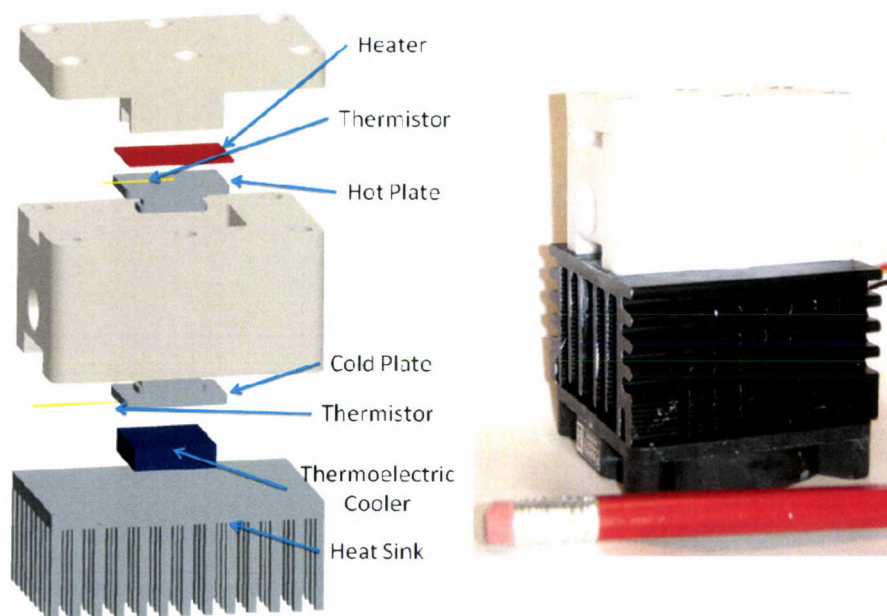


Figure 4. Three-dimensional model and photograph of the new thermophoretic sampler prototype.

The new device measures 5.0 cm by 3.2 cm by 7.4 cm (L x W x H), weighs 222.4 g, and consumes approximately 7.2 W of power during normal operating conditions. Power is supplied to the device using a rechargeable, 12V lithium-ion battery and a custom, high efficiency power circuit (Analog Devices, Inc., Fort Collins, CO). The lithium battery weighs 678 g, as compared to the three heavy lead-acid batteries used with the previous prototype (Section 3.5). Battery power is supplied to the device using a cat5e cable so that the controller and battery can be worn on a belt, away from the thermophoretic sampler. A photo of the device worn with the pump, battery, and controller is shown in Figure 5.



Figure 5. Photograph of the thermophoretic sampler as typically worn on a human torso.

The thermophoretic collection surface (i.e. the cold plate in Figure 4) measures 13 mm by 5 mm, and is cooled with a small, low-power thermoelectric cooler (TE Technology Inc., Traverse City, MI). The hot plate is heated with a 0.10 mm diameter Nichrome wire heater, which is electrically insulated with 0.0254 mm thick polyimide (Kapton) plastic adhesive sheets.

Nichrome was chosen because its resistivity enabled a 127 mm wire to dissipate 3.20 W of heat with a DC voltage drop of 8 V.

Temperatures of the cold and hot plates are maintained at 12.2 °C and 122°C, respectively, via a programmable temperature controller (TE Technology, Traverse City, MI) in conjunction with two small thermistors (TE Technology, Traverse City, MI). The cold plate temperature was chosen to minimize condensation in the device, while maximizing the temperature gradient (100,000 °C/m). The hot plate temperature was constrained to 122°C for safety considerations. A small heat sink with an integrated electric fan dispersed the heat generated by the thermoelectric cooler.

The chamber inlet was chosen to measure 5 mm wide by 1 mm high to match the plate width and separation distance, respectively. A 1 mm separation distance also maximized the temperature gradient while maintaining reasonable tolerances for machining and assembly of the components. Since air velocity is inversely proportional to cross-sectional area (0.05 cm²), a low flow rate was chosen to maintain laminar flow through the chamber. The velocity must also allow sufficient residence time for particles in the chamber to deposit under the action of thermophoresis. For these reasons, the thermal precipitator was operated at a flow rate of 5 mL/min. Calculations supporting the design of the thermophoretic collection chamber are provided in Section 4.2.

The main body and lid were constructed of polytetrafluoroethylene (PTFE), which has a low thermal conductivity (0.25 W/m·K) and a melting point of 260°C. The hot and cold plates were machined from aluminum, which has a high thermal conductivity (237 W/m·K). The cold plate was polished to create a smooth, uniform collection surface. The particle collection chamber was sealed with silicone o-rings, which were stretched around the base of the hot and cold plates, as shown in Figure 6.

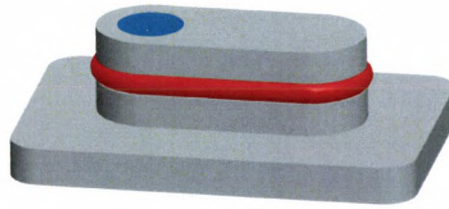


Figure 6. Three-dimensional model of the 19 mm by 12 mm by 5.5 mm (L x W x H) particle collection plate with magnet and O-ring seal.

2.2 Device Calculations

Design calculations were carried out to estimate particle collection efficiency and particle deposition location as a function of air temperature, flow rate, and height of entry (above the cold plate). Calculations were conducted to predict the maximum horizontal distance (following the direction of prevailing air flow within the collection chamber) that particles would travel before depositing on the collection plate. The separation distance between the hot and cold plate, H_{xs} , which was chosen to maximize the temperature gradient (as discussed in the previous section), constrained many of the dimensions chosen for the thermophoretic sampler flow channel. The horizontal flow velocity, V_{flow} , and vertical thermophoretic velocity, V_{th} , determined the horizontal deposition distance for particles entering at the top of the inlet. An illustration of the parameters used for this calculation is provided in Figure 7 (not to scale).

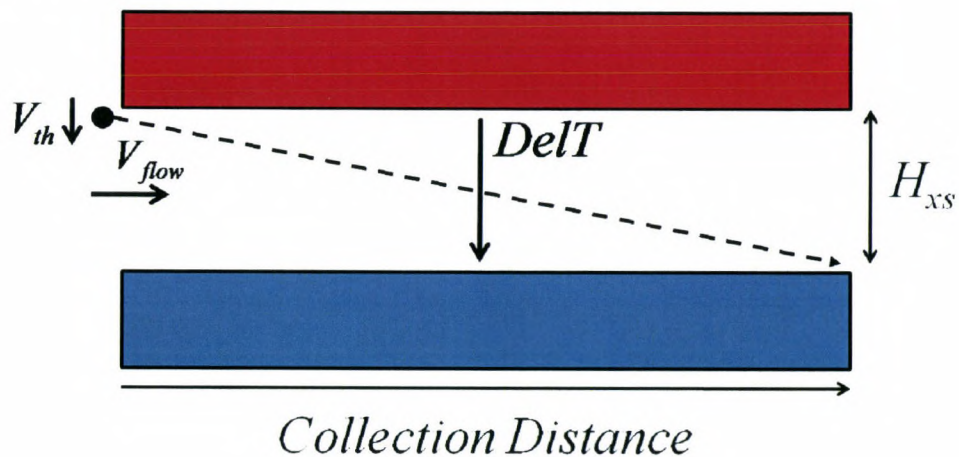


Figure 7. Model parameters used to calculate the particle collection distance.

Thermophoretic velocity depends on air viscosity, which varies with temperature, so calculations were performed for the cold plate and hot plate temperatures (12.2 °C and 122°C, respectively) to determine the deposition distance limits. These two values bound the thermophoretic velocity of the nanoparticles as they migrate across the temperature gradient, leading to a range of particle deposition velocities (and locations). This range helped to determine the length of the collection chamber that would result in 100% particle collection efficiency.

Although the principle behind thermophoresis is conceptually simple, modeling the process mathematically is complicated. Theoretically, the thermophoretic force, F_{th} , acting on a particle with diameter d can be estimated as:

$$(1) \quad F_{th} = \frac{-p\lambda d^2 \nabla T}{T}$$

where p is the gas pressure, λ is the gas mean free path, ∇T is the temperature gradient, and T is the temperature of the particle (Hinds, 1999). Equation (1) is generally valid when particle diameter is smaller than the gas mean free path. The mean free path of an ‘air molecule’ is approximately 66 nm at normal temperature and pressure. The corresponding thermophoretic velocity, V_{th} , for particles with diameters smaller than the gas mean free path is independent of particle size and is estimated by:

$$(2) \quad V_{th} = \frac{-0.55\eta \nabla T}{\rho_g T}$$

where η is the viscosity of the gas and ρ_g is the density of the gas (Hinds, 1999). Equation (2) is obtained by setting the Stokes drag force, F_D , equal to the thermophoretic force. Both force equations are dependent on d^2 , so the terms cancel out and the resulting equation is independent of particle size. For particles of standard density in a temperature gradient of 100,000 °C/m and a flow rate of 5 mL/min, particle residence times range from 0.518 s to 0.609 s (based on the thermophoretic velocity calculated using the temperature of the particle and the air viscosity at 22

and 122 °C). These residence times correspond to deposition distances ranging from 8.63 to 10.16 mm for a hypothetical particle entering the device at a height of 1 mm above the collection surface. Details of these calculations are provided in Appendix B.

Larger particles develop an internal temperature gradient, resulting in a more complex equation for the thermophoretic force. For particles larger than the gas mean free path, the thermophoretic force depends on the ratio of the thermal conductivity of the particle, k_p , to the thermal conductivity of the air, k_a :

$$(3) \quad F_{th} = \frac{-9\pi d \eta^2 H \nabla T}{2\rho_g T}$$

where the coefficient H accounts for the temperature gradient within the particle (Hinds, 1999).

An estimate of the coefficient H is given by Brock (1962) (qtd. in Hinds, 1999):

$$(4) \quad H \cong \left(\frac{1}{1 + \frac{6\lambda}{d}} \right) \left(\frac{\frac{k_a}{k_p} + 4.4 \frac{\lambda}{d}}{1 + 2 \frac{k_a}{k_p} + 8.8 \frac{\lambda}{d}} \right)$$

The steady state, or terminal, thermophoretic velocity is obtained by setting the Stokes' drag force equal to the thermophoretic force, resulting in the following relationship:

$$(5) \quad V_{th} = \frac{-3\eta C_c H \nabla T}{2\rho_g T}$$

The Cunningham slip correction factor, C_c , as developed by Allen and Raabe (1982), is defined as (qtd. in Hinds, 1999):

$$(6) \quad C_c = 1 + \frac{\lambda}{d} \left(2.34 + 1.05 e^{\left(\frac{d}{\lambda} \right)} \right)$$

Based on these calculations (see Appendix C), for a temperature gradient of 100,000 °C/m and a flow rate of 5 mL/min, a range of residence times of 0.406 s to 0.453 s was predicted.

These residence times correspond to deposition distances ranging from 6.77 mm to 7.55 mm downstream of the chamber inlet. Calculations for larger particle diameters ($d > \lambda$) are provided in Appendix C.

Flow through the chamber must be laminar for these equations to be accurate. The Reynolds number represents the ratio of inertial to viscous forces within a flow, given by:

$$(7) \quad \text{Re} = \frac{\rho_g V d}{\eta}$$

where V is the velocity of air around the particle or through the duct (Hinds, 1999). Equation (7) applies to flow around particles or through ducts, where d represents the characteristic dimension of interest. Laminar flow corresponds to Reynolds numbers (Re) less than 2,000 for flow through ducts. In this case, d is either the diameter of the particle or the diameter of the duct. The Reynolds number for both cases is much less than 2,000, indicating laminar flow through the collection channel. Calculations for the Reynolds numbers in each of the two equation sets above are included in Appendices B and C. Based on the calculations described above and detailed in the Appendices, the device was expected collect particles with 100% efficiency.

Calculations for particle collection efficiency were also conducted for a sample flow rate of 20 mL/min at the same temperature gradient as noted above (100,000 °C/m). Using Equation (1), a range of deposition distances of 34.5 mm to 40.6 mm was predicted. Using Equations 4-6, a range of deposition distances of 27.1 mm to 30.2 mm was predicted. The Reynolds numbers calculated for the velocities associated with this flow also verified laminar flow. These calculations are provided in Appendices B and C.

Nanoparticles diffuse rapidly in air and may deposit on the walls of the sampler inlet and collection chamber during sampling. Therefore, calculations (and subsequent experiments) were conducted to estimate particle diffusion losses as a function of particle size. The results of these calculations are summarized in Figure 8.

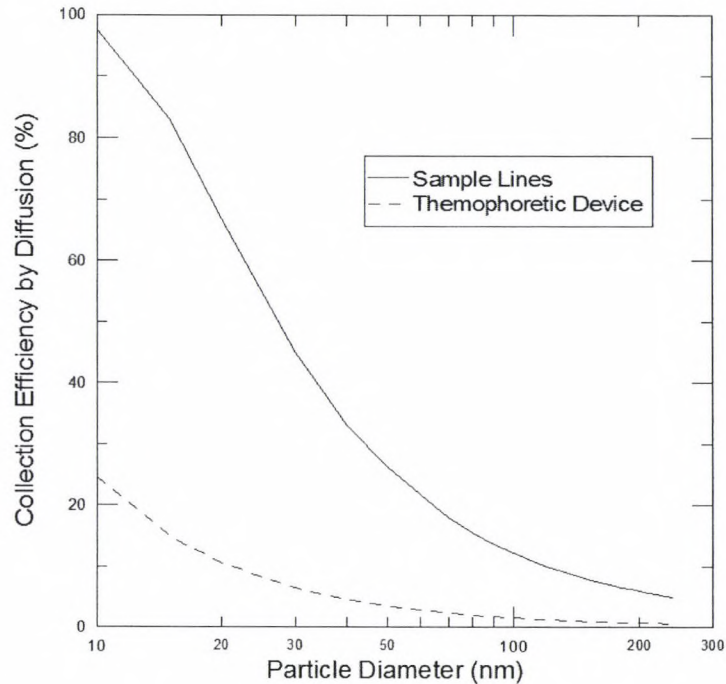


Figure 8. Estimated particle diffusion losses for the (6.35 mm ID, 635 mm long) sample lines and the thermophoretic sampler.

2.3 Experimental Setup

2.3.1 Collection Efficiency: 5 mL/min and 20 mL/min Flow

A series of experiments were conducted to measure the collection efficiency of the prototype thermophoretic sampler. The purpose of these experiments was to verify that a sufficient percentage of particles entering the device could be collected for subsequent analysis. Allowable concentrations or other dose metrics for nanoparticle exposure have not yet been determined, so high collection efficiency is desirable. The setup used for this test procedure is shown in Figure 9.

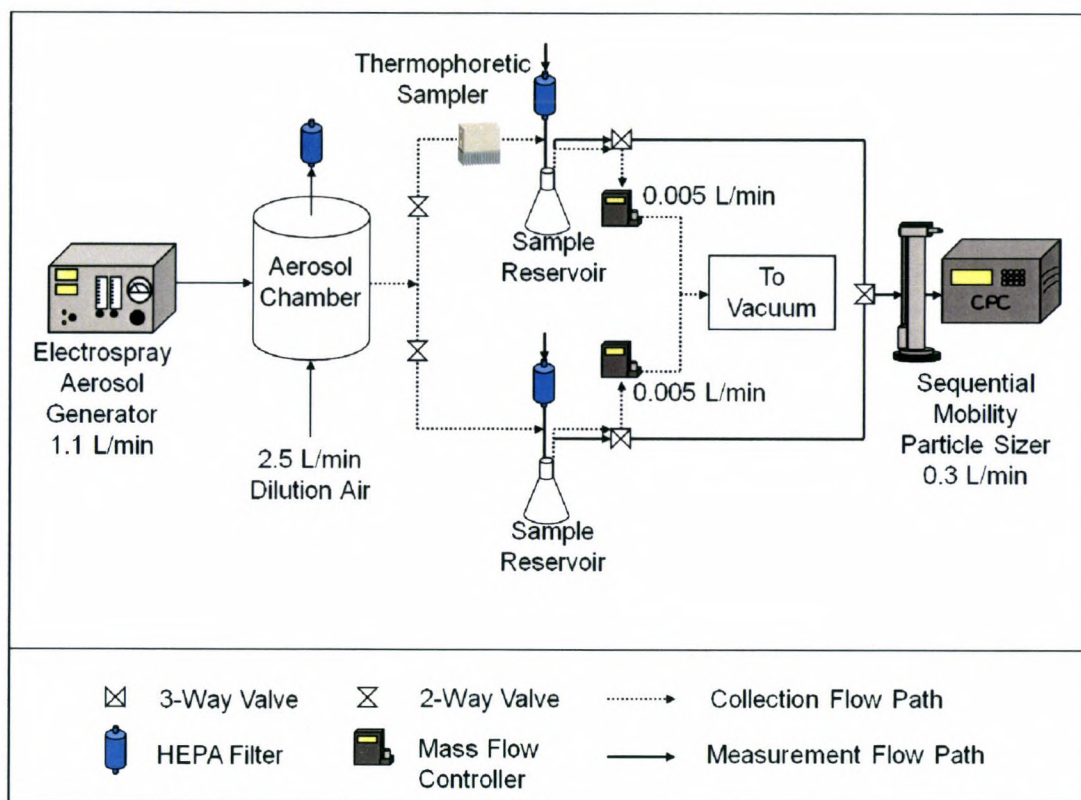


Figure 9. Experimental setup of the collection efficiency tests.

Since the reference measurement instrument (described below) cannot sample at the same low flow rate as the thermophoretic device (5 mL/min), a pair of 2 L jars were set up in parallel as delayed sample reservoirs. These reservoirs were initially cleared of contaminating aerosol by purging with a high flow of particle-free air for 10-15 minutes. A sequential mobility particle sizer (GRIMM Aerosol Technik, Ainring, Germany) was used to determine the concentration and size of particles within each sample reservoir.

A sequential mobility particle sizer consists of a differential mobility analyzer used in conjunction with a condensation particle counter and computer software. Aerosol enters the differential mobility analyzer through a neutralizer containing a radioactive source, which places a Boltzmann charge distribution on the particles before they enter the main chamber. The main chamber consists of a charged rod located concentrically within a grounded flow tube. Application of a regulated voltage to the central rod creates a uniform electric field in the air gap

between the rod and tube. Charged particles enter near the outer wall of the cylinder. Like charges are repelled towards the outer wall and opposite charges are drawn towards the rod. Charged particles with high electrical mobility impact on the rod, while particles with low electrical mobility simply flow out of the tube. However, particles of a pre-defined electrical mobility (as regulated by the applied voltage) pass through a small exit slot near the end of the rod. The differential mobility analyzer, therefore, selects only particles within a narrow range of electrical mobility diameter, allowing only particles of a pre-determined narrow size range to pass into a condensation particle counter for subsequent counting.

A condensation particle counter is a light scattering device that can determine the number concentration of an aerosol in real time. However, particles with diameters smaller than the wavelength of light (~300 nm) typically do not scatter enough light for detection. Therefore, sampled aerosol is first passed through a condensation chamber to grow particles to a sufficient size until they can be individually counted using light scattering. A condensation particle counter cannot differentiate particle size, but when used in conjunction with a differential mobility analyzer and computer software, particle number concentration as a function of size can be measured.

Nanometer-sized, monodisperse test aerosols ($d < 100$ nm) were created from a sucrose solution using an electrospray aerosol generator (TSI Inc., Shoreview, MN). In the device, sucrose dissolved in a buffer solution is pushed through an open-ended capillary tube, forming a droplet at the tube exit. As voltage is applied to the tube, a surface charge forms on the droplet. When the charge on the droplet reaches the Rayleigh limit, the droplet explodes into a fine cloud of multiply-charged, monodisperse droplets. The Rayleigh limit is a bound for liquid droplets which depends on the surface tension of the liquid. When the repulsive force of multiple electric charges on a droplet exceeds the surface tension of the droplet, the droplet shatters into many smaller droplets to redistribute the charge over a larger surface area. These droplets are mixed with dilution air in a separate chamber to dry them, thus producing a high concentration,

monodisperse, test aerosol. These droplets are immediately directed past an aerosol neutralizer to reduce their net charge to a Boltzmann-like distribution.

Larger test aerosols ($d > 100$ nm) were generated using a Collison nebulizer and polystyrene latex (PSL) spheres (Duke Scientific Corp., Palo Alto, CA). A Collison nebulizer uses a jet of pressurized air to atomize a solution located within a liquid reservoir. Liquid is entrained into the air jet by virtue of a venturi, connecting the reservoir to the jet nozzle. Atomized droplets exit the nebulizer and pass a silica gel dessicant tube to evaporate the water, leaving the particles from the solution suspended in the air.

The air flow from the dilution chamber or dessicant tube was split into two lines that ran in parallel to the sample reservoirs (Figure 9). These two lines were identical in length and kept as straight as possible to minimize particle losses. The thermophoretic sampler was placed in line with one of the jars, while the second jar acted as a control reservoir. Aerosol flow to the sample reservoirs was applied with laboratory vacuum and regulated using mass flow controllers (Omega Engineering, Inc.). The flow rate through the sample lines was verified using a Bubble-O-Meter (Bubble-O-Meter, LLC., Dublin, Ohio) and stopwatch while the aerosol chamber was filled with monodisperse nanoparticles. The reservoirs were filled for 3-5 hours for PSL to generate sufficient concentrations ($\sim 800/\text{cm}^3$) for SMPS measurement. Conversely, the electrospray generated very high concentrations of particles ($\sim 13,000/\text{cm}^3$), so collection tests lasted as little as 20 minutes to fill the jars to an acceptable level for measurement. Inconsistent aerosol generation required longer times (up to 3 hours) for some tests using the electrospray aerosol generator.

After the sampler reservoirs had filled, the sequential mobility particle sizer was used to measure the aerosol concentration in each reservoir, with multiple measurements alternating between reservoirs. The difference in concentration between the jars was used to calculate the collection efficiency of the device. The average and standard deviation of the measured collection efficiency was calculated for each particle size. A summary of the test parameters for the collection efficiency tests is presented in Table 1.

Variable	Level Investigated
Particle Size (nm)	15, 51, 100, 240
Flow Rate (L/min)	0.005, 0.020
Replicates, Each Test	3
Aerosol Type	PSL, Sucrose
Test Duration (hrs)	0.3 - 5

Table 1. Experimental Conditions for Particle Collection Efficiency Tests with an Applied Temperature Gradient.

Tukey's HSD method for multiple comparisons among means was used to determine whether significant differences existed for particle collection efficiencies as a function of particle size. Multiple-comparison tests allow for pair-wise comparisons without increasing the probability of Type 1 error (falsely concluding a difference exists), which would be the case if pair-wise comparisons were made using individual t-tests. All statistical tests were conducted using Minitab statistical software (Minitab, Inc., State College, Pennsylvania) with a Type 1 error rate (α) of 0.05. Confidence intervals for the difference in means for each pair-wise comparison were calculated. If the difference between means is less than the calculated HSD value, then the means are not statistically different.

2.3.2 Diffusion Loss Tests: 6.7 mL/min Flow

The collection efficiency test procedure was repeated with the device off to establish a worst-case estimate for wall losses in the device due to particle diffusion. Since the mass flow controllers were inconsistent at these low flow rates, they were replaced with critical flow orifices (Lenox Laser, Glen Arm, MD) for these tests. The orifices had a custom, laser cut diameter of 26 nm (actual values reported by the company were 27.20 and 26.92 nm), with a measured flow rate of approximately 6.7 mL/min. These tests were only performed at this flow rate, since losses would be lower at higher rates, and the purpose of the test was to determine an upper estimate of diffusion losses. Furthermore, only the three smallest particle sizes were tested, since diffusion losses are expected to decrease dramatically with increasing particle size (Hinds, 1999). As with

the previous test, the average and standard deviation were calculated and plotted for the 6.7 mL/min flow rate data. A summary of the test parameters for the collection efficiency tests at this flow rate is presented in Table 2. Again, Tukey tests were used to determine whether the data were statistically different.

Variable	Level Investigated
Particle Size (nm)	15, 30, 60
Flow Rate (L/min)	0.0067
Replicates, Each Test	3
Aerosol Type	Sucrose
Duration (hrs)	3

Table 2. Experimental Conditions for Particle Collection Efficiency Tests Without an Applied Temperature Gradient.

2.3.3 Collection Uniformity Tests

A third set of tests was performed to determine the homogeneity of particle collection across the collection plate surface. If the flux of particles to the cold plate is uniform, then the concentration and size distribution can be reconstructed from relatively few SEM images. For these tests, the same procedure for the collection efficiency tests was used but the parallel sample reservoir was not used. A sketch of this test setup is shown in Figure 10.

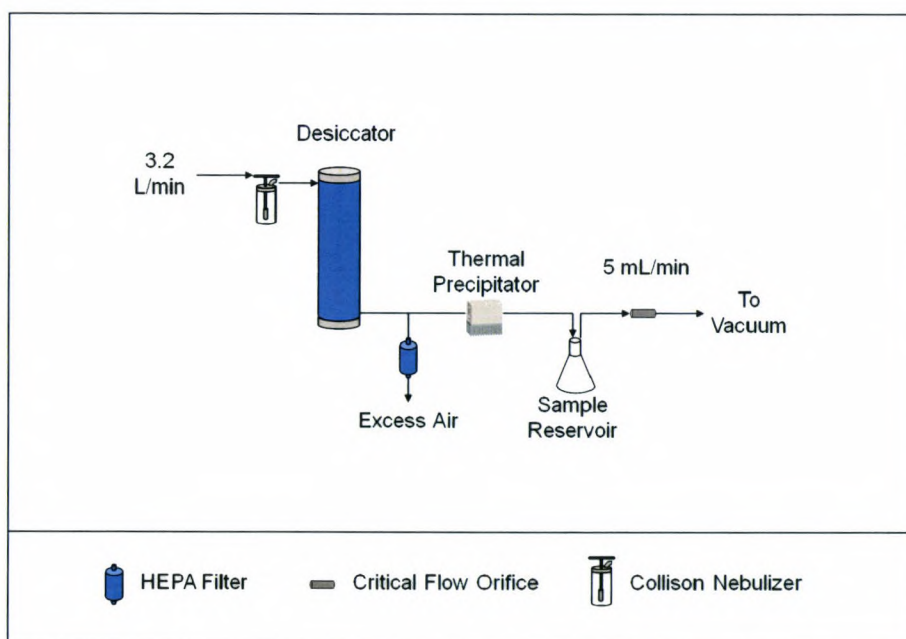


Figure 10. Experimental setup of the collection uniformity tests.

In this configuration, each test was performed for 6 hours, using a 0.1% salt solution in the Collison nebulizer. The particle concentration in the reference reservoir was measured at the end of one of these tests to verify that the device still collected 100% of the particles entering the collection chamber. The salt solution generated a polydisperse aerosol with an average count median diameter of 30.8 nm and an average geometric standard deviation of 2.01 nm. After 6 hours of collection, the aluminum collection plate was placed in a petri dish and sealed with PTFE tape prior to SEM analysis. A series of ten SEM images was taken across the width of the collection plate at distances of 2, 3.75, 5.5, 7.25, and 9 mm downstream of the inlet, as shown in Figure 11. These locations were referenced in the SEM by scoring the outside of the collection plate at each of the aforementioned locations.

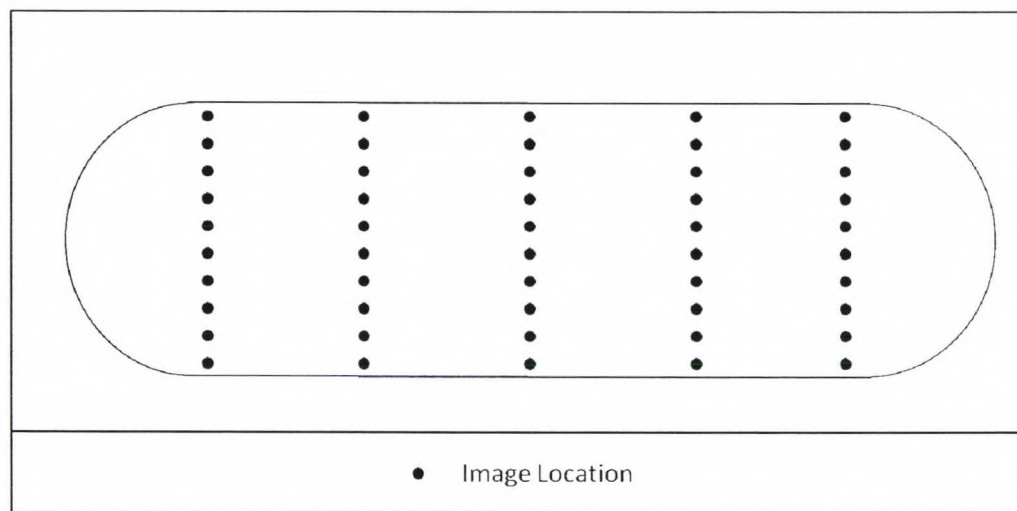


Figure 11. SEM imaging locations on the particle collection surface.

Since the location of the SEM camera can be controlled by entering specific x-y coordinates, an Excel file was generated to calculate ten equidistant picture locations along a line for each area on the aluminum surface. A summary of the variables for the collection efficiency tests at this flow rate is presented in Table 3.

Variable	Level Investigated
Particle Size Bins (nm)	25-40, 41-65, 66-200
Flow Rate (L/min)	0.0067
Replicates, Each Test	3
Aerosol Type	Salt
Duration (hrs)	6

Table 3. Experimental Conditions for Collection Uniformity Tests.

After imaging the particles under the SEM, ImageJ (Rasband, 1997-2009) software was used to sort the particles into diameter ranges of 25 to 40, 41 to 65, and 66 to 200 nm. The software was then used to count the number of particles in each range. The procedure for counting particles is provided in Appendix D. The counts were mean-normalized, averaged, and graphed on a contour plot to determine homogeneity of particle deposition across the collection surface. To normalize the data, the average number of particles per image was calculated for each particle size. The relative difference (i.e. percent deviation from the mean) was calculated from this value at each location and averaged for the three trials. A contour plot was constructed from the average values to visualize the spatial distribution of collected particles as a function of size.

Although 15 nm particles were of interest in previous tests, this size was excluded since the SEM cannot reliably image particles of this size.

3 Results

3.1 Collection Efficiency: Device On, 5 mL/min Flow

Particle collection efficiencies for a flow rate of 5 mL/min are presented in Figure 12, which is a plot of measured collection efficiency as a function of particle diameter for 3 different operating conditions (5 mL/min, 20 mL/min, and 6.7 mL/min with zero temperature gradient).

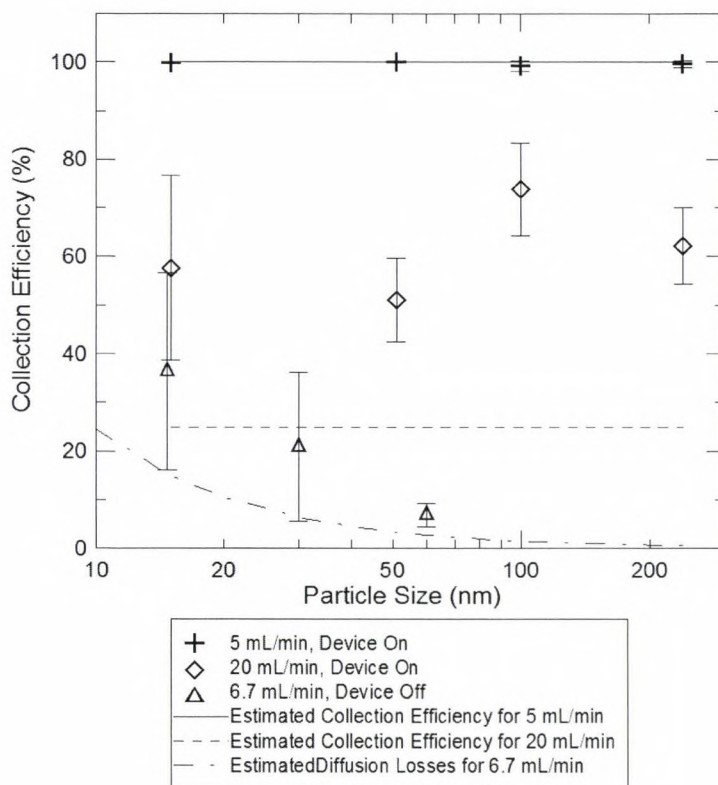


Figure 12. Measured collection efficiencies as a function of particle size and flow rate.

Error bars represent one standard deviation. The solid plotted line represents the predicted values for a 5 mL/min flow rate. The dashed line represents the predicted

values for a 20 mL/min flow rate. The dash-dotted line represents the predicted values for diffusion losses at a flow rate of 6.7 mL/min.

The points on the graph represent the averaged collection efficiency for each particle size. The error bars represent one standard deviation based on multiple, repeat tests. The average collection efficiency for the 15 nm particles was determined to be 99.8%. The data have a very small variance in relative collection efficiency, with a standard deviation of 0.11%. The 51 nm particles were collected with an average of 100% collection efficiency. The data recorded for this size also have a very small standard deviation of 0.0016%. The collection efficiency for the 100 nm particles was calculated to be 99.27%, with a standard deviation of 0.85%. The average collection efficiency for the 240 nm particles is 99.58%. These data have a calculated standard deviation of 0.59%. Differences in the length of the collection phase of testing had no effect on the relative collection efficiency for each particle size. A Tukey test performed on the data shows no significant differences in the collection efficiencies among the particle sizes measured in this experiment for a sample flow rate of 5 mL/min ($p = 0.717$).

3.2 Collection Efficiency: Device On, 20 mL/min Flow

Results of the 20 mL/min collection efficiency tests are also shown in Figure 12. At this flow rate, 15 nm particles were collected with 57.63% efficiency. The standard deviation for these data was 19.02%. The collection efficiency for the 51 nm particles was 51.13% with a standard deviation of 8.63%. The 100 nm and 240 nm aerosol were collected with an efficiency of 73.88% and 62.24%, respectively, with standard deviations of 9.57% and 7.82%. The Tukey test for these data also showed no significant differences among collection efficiencies at the 20 mL/min flow rate ($p = 0.212$).

3.3 Diffusion Loss Tests: 6.7 mL/min Flow

Particle collection efficiencies at 6.7 mL/min with the device turned off is shown in Figure 12. Without an applied temperature gradient, 15 nm particles were collected with an average efficiency of 36.46% with a standard deviation of 20.29%. Measured diffusion losses for 30 nm particles was 20.91% with a standard deviation of 15.32%. The average collection efficiency for 60 nm particles with the device off was 6.87% with a standard deviation of 2.34%.

Visual inspection of the collection efficiency plot suggests that the data for a sample flow rate of 6.7 mL/min do not have homogeneous variability, which is assumed for Tukey's test. Hence, a Box-Cox test was conducted to determine whether a data transformation was necessary. The Box-Cox test indicated that a log-transformation was necessary to make the data homoscedastic. The log-transformed data satisfied the assumption of homogeneity of variance, as required by the Tukey test. Results of the Tukey test for the transformed data are presented in Table 4.

Size ($\mu_1 - \mu_2$)	Difference in Means	Significant Difference? (HSD = 0.662)
15 nm – 30 nm	0.9488	Yes
15 nm – 60 nm	0.7153	Yes
30 nm – 60 nm	0.4290	No

Table 4. Tukey's HSD multiple comparison test for log transformed 6.7 mL/min data.

The difference in the geometric mean for 15 nm is significantly different from the mean for 30 nm and 60 nm ($p = 0.043$).

3.4 Collection Uniformity Tests

A plot depicting the uniformity of particle deposition across the cold plate collection surface is shown in Figure 13.

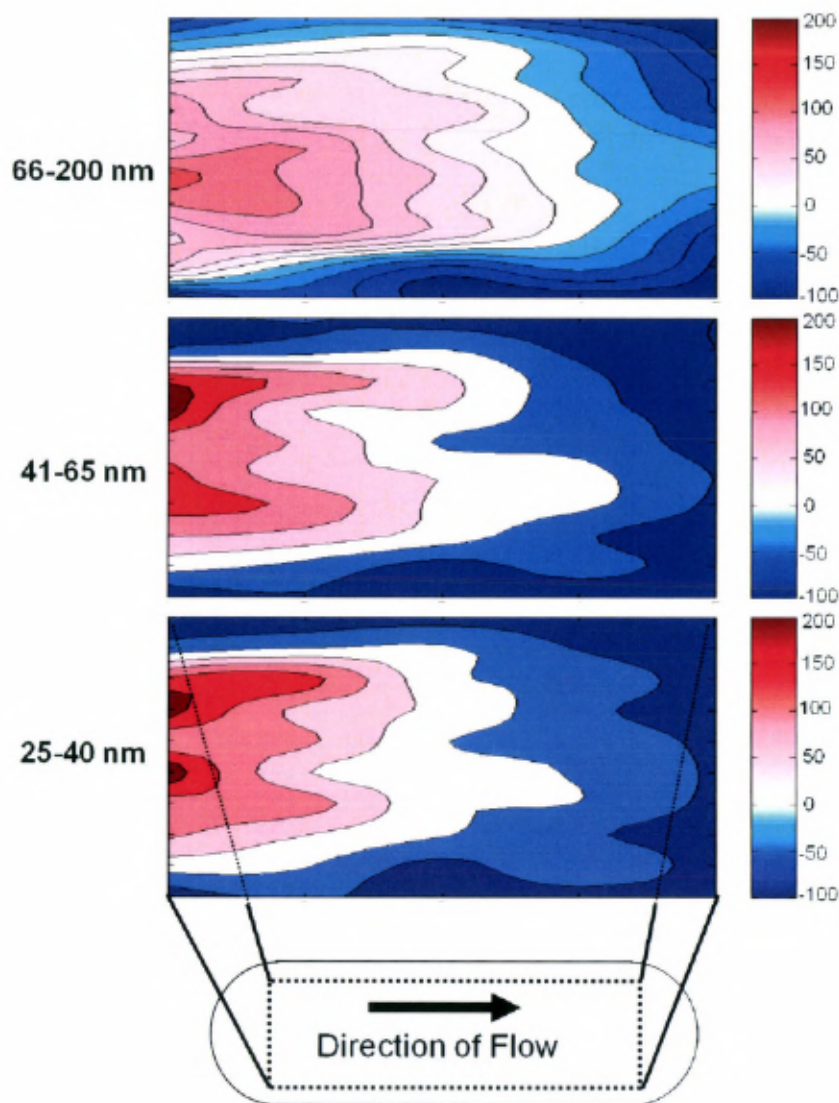


Figure 13. Uniformity of particle deposition across the collection surface as a function of particle size. Red and blue contours represent positive and negative deviations from the average surface count (number/area), respectively. The x- and y-axes define the particle collection area, as shown in the inset. Each image represents an average of three repeat tests.

Depicted in the figure are particle counts (relative to the average) for the three repeated tests. The white contours represent the average particle counts per image for all of the data. Red and blue contours indicate a positive or negative percent difference from the average counts per image,

respectively. The average relative standard deviation was 4.4% for the 25 to 40 nm particles, 1.8% for the 41 to 65 nm particles, and 2.0% for the 66 to 200 nm particles. Example SEM images from three areas of the collection plate are shown in Figure 14.

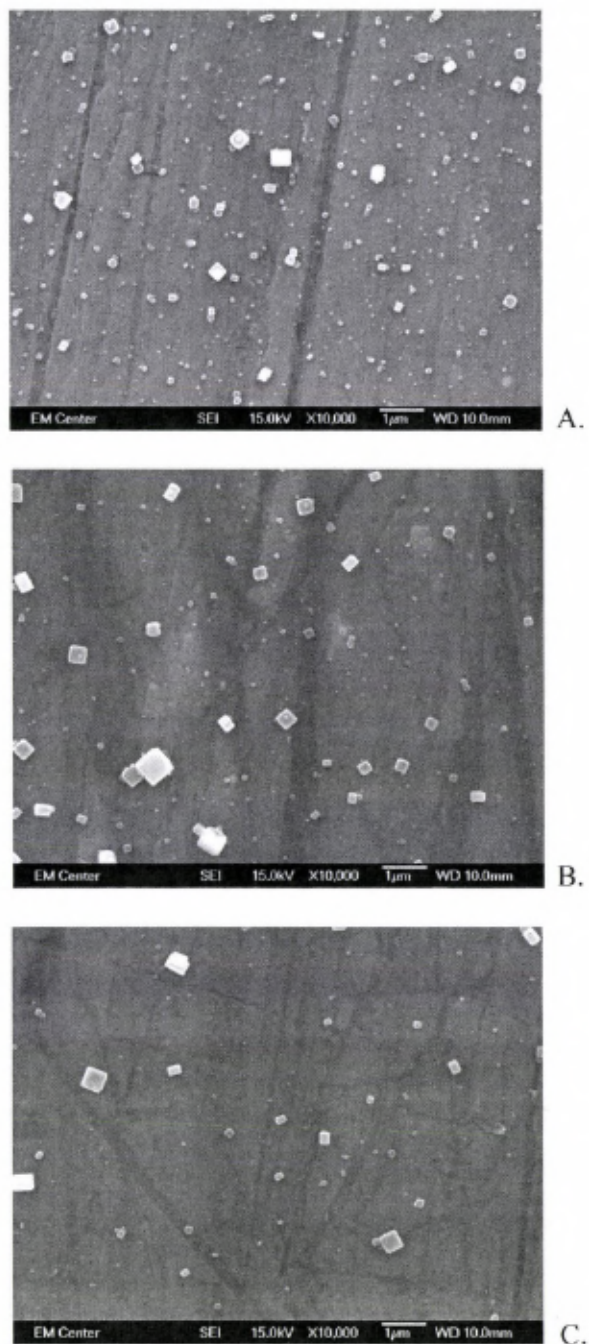


Figure 14. Example SEM images from the centerline of the particle collection plate. A) Near the collection chamber inlet. B) At the center of the plate. C) Near the collection chamber outlet.

4 Discussion of Results

4.1 Collection Efficiency: Device On

At 5 mL/min, the thermal precipitator collected particles with near 100% efficiency. These results validate the calculations conducted during the design phase, indicating that the thermophoretic sampler is effective at capturing particles from 15 to 240 nm in diameter. Higher collection efficiencies support a more precise exposure assessment by reducing the uncertainty associated with calculating breathing-zone concentrations of airborne nanoparticles. However, since the number of particles collected scales with the product of flow rate and collection efficiency, lower flow rates may be desired, especially if method sensitivity is important. For example, some toxicity studies indicate that very small levels of exposure result in adverse health effects.

The values for 5 mL/min sample flow rate are the results of early tests (at the start of this study) when the most effective test procedure had not yet been determined. However, it is highly probable that these collection efficiency values are still accurate, because a 100% collection efficiency calculation results from a 0 particles/cm³ measurement from the device sample reservoir. A 0 particles/cm³ measurement would give the same result regardless of the procedure, provided the jars were clean at the start of the test. These calculated efficiencies also had a very small standard deviation, which means that very similar calculated relative collection efficiencies were obtained despite variations in test procedures. The small variation in data for a sample flow rate of 5 mL/min is a result of the very high collection efficiency, which also makes the device very precise. Since nearly 100% of the sampled particles are collected, analysis (such as counting with imaging software) will give an accurate representation of the original sample.

When the thermophoretic sampler was operated at a flow rate of 20 mL/min, the measured collection efficiency data had much greater variability, and hence greater uncertainty. Therefore, the precipitator is less precise when operated at a higher flow rate.

For a flow rate of 20 mL/min, the collection efficiency of the device dropped to between 50% and 70%. Since the length of the collection plate spans approximately one quarter of the predicted deposition distance (30 to 40 mm at 20 mL/min), a drop in collection efficiency of approximately 75% was expected at the 20 mL/min sample flow rate. This prediction is based on the assumption that particle deposition is uniform along the cold plate. However, the deposition uniformity tests indicate that the majority of nanoparticles collect near the leading edge of the cold plate, so small increases in flow rate would not increase losses by a large amount. Additional curves depicting the variation in collection efficiencies over a range of flow rates may be useful. For example, if lower concentrations are anticipated during measurement in a study, the flow rate can be increased (to increase sensitivity) and correction factors can account for the inefficiency of the thermophoretic sampler (twice the number of particles are collected by increasing the flow rate from 5 mL/min to 20 mL/min over the same collection period, accounting for a 50% collection efficiency). However, at a higher flow rate, only relatively large differences in the concentration will be detected, due to uncertainty in particle collection efficiency.

Decreased collection efficiency at increased flow rate is a result of the increase in air velocity and a decrease in residence time for the particles within the collection chamber. As flow velocity increases, particles entering the collection chamber have less time to reach the collection surface before exiting with the flow at the rear of the chamber. Higher flow rates may be desirable for several reasons. For example, a wider variety of pumps are available at 20 mL/min and greater flows. In addition, increasing the flow from 5 to 20 mL/min only resulted in 30% to 50% reduction in collection efficiency, meaning that more particles are collected at higher flow rates, for a given sampling duration.

The mass flow controllers used for this experiment are designed to operate from 0-100 mL/min. Tests conducted at 5 mL/min flow were near the lower limit of the controller's capability, which may have increased the variability in flow rate. Although the flow varied substantially (as much as a 20% difference from 5 mL/min) for the 5 mL/min flow rate tests, very little variation was observed in the data since the collection efficiencies were near 100%. Similar variation in the 20 mL/min flow rate was observed (up to a 16% difference from 20 mL/min). The use of critical flow orifices provided a more stable flow rate using the vacuum in the laboratory. However, since the thermophoretic sampler is intended to be worn as a personal sampler, a small pump that supplies a reliable flow rate is critical to future designs.

The multiple, pair-wise comparisons using Tukey's HSD method showed no variation between the observed means in collection efficiency for each particle size. This result was expected, since the device was designed to collect all particle sizes with 100% efficiency at 5 mL/min. Tukey's HSD tests also showed no variation between collection efficiency and particle size at a flow rate of 20 mL/min. This result was also expected, since the thermophoretic velocity is nearly independent of particle size in the nanoparticle range. Increasing the flow rate was not expected to change the variation in the data.

4.2 Diffusion Loss Tests: 6.7 mL/min Flow

Aerosol diffusion losses tend to decrease with increasing particle size, since smaller particles are more affected by Brownian motion than larger ones. The collection efficiency measurements with the device off should overestimate particle diffusion losses, since the thermophoretic force is created by differential Brownian forces at the particle surface. Brownian motion will still result in nanoparticle deposition on the walls and hot plate while the thermophoretic device is operating. However, thermophoresis is a special case of Brownian motion, in which the overall, "random" motion from air molecule collisions is directed down the temperature gradient. The losses from deposition on the wall and hot plate are still very high (approximately 40%) for very small

nanoparticles, but rapidly decrease to relatively low levels (less than 10% of the collection efficiency for a 5 mL/min flow rate) for larger particles. However, losses from particle diffusion were higher on average than the calculated values, with the exception of the 60 nm particle losses. The standard deviations for these calculations were quite large, but these results may be improved with more measurements, since only three tests were completed. Some measurements were close to the predicted losses, while others were significantly larger, which may have been caused by errors made during data collection.

The data collected for these tests was highly variable, despite the use of critical orifices to supply a consistent flow rate. The variation in data was a result of two artifacts of sampled concentration that occur as the reservoirs empty during measurement with the sequential mobility particle sizer. First, since the reservoirs are sealed once the measurement is complete, particle concentrations in each reservoir decreases exponentially as the aerosol is sampled by the sequential mobility particle sizer. Since only one sequential mobility particle sizer was used, the two reservoirs could not be sampled simultaneously, resulting in increased diffusional losses for the reservoir sampled second. As the aerosol is depleted, the concentrations in both reservoirs asymptotically approach zero. At this point, the concentration difference between the reservoirs is negligible. The time available for scanning with the sequential mobility particle sizer varies daily, depending on the initial aerosol concentration. This variability could possibly be decreased by using only the first few pairs of measurements taken by the sequential mobility particle sizer. Another possible source of uncertainty was caused by human error in timing of the three-way valve operation. This resulted in unequal time spent scanning each reservoir, leading to increased variability in the measured aerosol concentration.

The Box-Cox test showed that the data most closely follows a log-regression. Although this does not match Hind's (2005) model used to predict collection by diffusion, the result agrees with

the expectation that the data is nonlinear. In addition, even though the geometric means were used for the multiple, pair-wise comparisons, the results still suggest that the original means are significantly different.

4.3 Collection Uniformity Tests

Collected particles were distributed most densely at the entrance of the collection chamber and along the center of the collection plate for all three particle size ranges. The increased particle counts in the center of the plate may have been caused by a non uniform temperature gradient between the plates. Heat transfer at the boundary between the aluminum plates and the PTFE case could cause the temperature gradient to decrease away from the center of the plate, which would result in a lower thermophoretic velocity at the chamber edges. The higher density of particle collection along the center line of the cold plate may have been a result of particle losses by diffusion in the tube leading to the thermophoretic device during testing. Particles may have been concentrated in the center of the tube by higher diffusion losses at the tube walls during transport to the thermophoretic sampler, which is an artifact of the experimental setup. Such preferential concentration of aerosol along the centerline of sampled flow would not occur in the field, where the sampler would be open to the ambient air.

Since the relative standard deviation is less than 5% for all three particle sizes, the spatial distribution between tests is low, meaning that the particle flux to different areas of the collection plate is repeatable. Results from these tests also provide insight into the optimal location for an electron microscopy grid, as the sample grid should be placed in an area where the particle spatial distribution best represents the average particle distribution on the plate, which corresponds to white areas on the collection uniformity plots. The white contours are located approximately in the center of the collection plate for all three particle size ranges. Therefore, a TEM grid placed in the center of the collection plate will provide a sample containing approximately the average number particles per image over the entire nanoparticle size range (recall that nanoparticles are generally defined as particles with at least one dimension below 100 nm). TEM analysis of these

grids would provide the best estimate of the true number of sampled particles. Correction factors must also be determined to reconstruct the actual sampled aerosol concentrations from the particle counts obtained from electron microscopy analysis. Calculations using the known flow rate and particle counts from electron microscope images can provide an estimated reconstruction of the concentration measured by the thermophoretic sampler. The calculation results can be compared to the known concentration entering the device to infer a correction factor to account for losses within the device.

Particles greater than 40 nm seemed to collect more homogeneously than smaller particles. This may have been an artifact of the counting procedure. As mentioned previously, noise in the images from poor focus or small bright spots were often miscounted as small particles, which could have caused additional variation in the data that resulted in a larger relative standard deviation for particle counts below 40 nm.

5 Conclusions and Suggestions for Future Research

Personal samplers are needed to determine worker exposure levels and for use in toxicological studies focusing on newly developed nanoparticle aerosols. A thermophoretic nanoparticle sampler was designed and tested to meet this need. The new prototype is small and lightweight, measuring 5.0 cm by 3.2 cm by 7.4 cm (L x W x H) and weighing 222.4 g. The thermophoretic sampler also has reduced power requirements, using approximately 7.2 W supplied from a small battery designed to be worn on a worker's belt during a typical 8 hour work shift. These design specifications are acceptable for a personal sampling device. An aluminum collection plate served as a suitable SEM substrate to determine the size and morphology of sampled nanoparticle aerosol, which can be easily adapted to hold a TEM grid for alternative analyses.

Three primary experiments were conducted to test the performance of the thermophoretic sampler. Design calculations were verified by determining the particle collection efficiency from the measured difference between the concentration downstream of the device and an identical, parallel sample line without the device, which served as the reference. The near 100% collection efficiency calculated from the results for test aerosols with 15, 51, 100, and 240 nm diameters agreed with the design calculations. The test was repeated at a flow rate of 20 mL/min to determine the decrease in collection efficiency for a higher flow rate. Increasing the flow rate by a factor of four decreased particle collection efficiency by a factor of approximately two. This result suggests that the majority of particles collect near the entrance of the device, since an increase in flow rate by a factor of four would decrease the collection efficiency by a factor of four if the particles entering the thermophoretic sampler were homogeneously distributed. However, the thermophoretic sampler's accuracy and precision decreased dramatically with an increase in flow rate for the 20 mL/min flow rate.

Diffusion losses were estimated and measured while the device was turned off, so correction factors could be used to account for losses in the device. Although the measured losses were higher than estimated, the calculated values for losses were generally within one standard deviation of the experimental data. Additional diffusion loss tests may decrease the variance in these measurements.

Particles collected onto the cold plate were also analyzed to determine the homogeneity of collection using scanning electron microscopy and imaging software. Particle collection is generally homogeneous across the center of the collection plate over a distance of approximately 2 mm. This area also coincides with a 0% deviation from the average number of particles per image, which is the ideal location for the placement of the TEM grid. Visual analysis of the collection surface confirmed that the majority of particles collect near the beginning of the cold plate. It was noted that collection of particles that entered near the hot plate occurred at roughly the same distance on the cold plate for all particle sizes. Calculations to predict the effect of particle size on collection distance could be an area of future research.

The limitations of this study emphasize the need for additional tests. Only three repeats were performed for each test, and a wide variation in the data was observed. Although the current design allows for chemical analysis as a means to differentiate between incidental and engineered nanoparticles, no such analysis was completed. Further testing is needed to verify the performance of the aluminum collection plate as a substrate for chemical analyses. Additional collection tests outside of a laboratory setting (such as being worn on the lapel over an eight hour work shift) are also necessary to verify the performance of the device under more realistic operating conditions.

Finally, the current design may be refined and redesigned for improved performance. Future work should focus on adapting the thermophoretic device for time-resolved sampling. Time-resolved measurements could help determine the source of process-specific nanoparticle aerosols in the workplace, especially when such data is combined with records of specific tasks (e.g.

bagging nanomaterials or cleaning equipment) conducted during sampling. Three dimensional concepts have been modeled to adapt this prototype for time-based collection. However, none of these designs have been constructed and tested for performance. As with the current device, a new prototype would need to be small, lightweight, and adequately sealed to prevent leaks.

References

Arico AS, Bruce P, Scrosati B, Tarascon J, Schalkwijk WV (2005). "Nanostructured Materials for Advanced Energy Conversion and Storage Devices." *Nature* 4: 366-377.

Chan CK, Peng H, Liu G, McIlwrath K, Xiang XF, Huggins RA, Cui Y (2007). "High-Performance Lithium Battery Anodes Using Silicon Nanowires." *Nature Nanotechnology* 3: 31-35.

Dames P, Gleich B, Flemmer A, Hajek K, Seidl N, Wiekhorst F, Eberbeck D, Bittmann I, Bergemann C, Weyh T, Trahms L, Rosenecker J, Rudolph C (2007). "Targeted Delivery of Magnetic Aerosol Droplets to the Lung." *Nature Nanotechnology* 2: 495-499.

Fissan H, Neuman S, Trampe A, Pui DYH, Shin WG (2007). "Rationale and Principal of an Instrument Measuring Lung Deposited Nanoparticle Surface Area." *Journal of Nanoparticle Research* 9(1): 53-59

Fujitani Y, Kobayashi T (2008). "Measurement of Aerosols in Engineered Nanomaterials Factories for Risk Assessment." *Nano: Brief Reports and Review* 3(4): 245-249.

Fujitani Y, Kobayashi T, Arashidani K, Kunugita N, Suemura K (2008). "Measurement of the Physical Properties of Aerosols in a Fullerene Factory for Inhalation Exposure Assessment." *Journal of Occupational and Environmental Hygiene* 5(6): 380-389.

Furuuchi M, Choosong T, Hata M, Otani Y, Tekasakul P, Takizawa M, Nagura M (2010). "Development of a Personal Sampler for Evaluating Exposure to Ultrafine Particles." *Aerosol and Air Quality Research* 10: 30-37.

Gonzalez D, Nasibulin AG, Baklanov AM, Shandakov SD, Brown DP, Queipo P, Kauppinen E (2005). "A New Thermophoretic Precipitator for Collection of Nanometer-Sized Aerosol Particles." *Aerosol Science and Technology* 39: 1064-1071.

Han JH, Lee EJ, Lee JH, So KP, Lee YH, Bae GN, Lee SB, Ji JH, Cho MH, Yu I (2008). "Monitoring Multiwalled Carbon Nanotube Exposure in Carbon Nanotube Research Facility." *Inhalation Toxicology* 20(8):741-749.

Handy RG, Jackson MJ, Robinson GM, Lafreniere MD. (2006). "The Measurement of Ultrafine Particles: A Pilot Study Using a Portable Particle Counting Technique to Measure Generated Particles During a Micromachining Process." *Journal of Materials Engineering and Performance* 15(2): 172-177.

Hinds, William C. (1999). *Aerosol Technology: properties, behavior, and measurement of airborne particles-2nd ed.* New York: John Wiley & Sons, Inc.

Jong WHD, Borm PJA (2008). "Drug Delivery and Nanoparticles: Applications and Hazards." *International Journal of Nanomedicine* **3**(2): 133-149.

Maynard AD, Aitken RJ, Butz T, Colvin V, Philbert MA, Ryan J, Seaton A, Stone V, Tinkle SS, Tran L, Walker NJ, Warheit DB (2006). "Safe Handling of Nanotechnology." *Nature* **444**(16): 267-269.

Maynard AD and Kuempel ED (2005). "Airborne Nanostructured Materials and Occupational Health." *Journal of Nanoparticle Research* **7**: 587-614

Monica JC, Heintz ME, Lewis PT (2007). "The Perils of Pre-emptive Regulation." *Nature Nanotechnology* **2**: 68-70.

Nkwenti AW, Christof A, Burkhard S, Heinz F, Heinz K, Sabine P, Thomas AJK (2009). "Optimisation of a Thermophoretic Personal Sampler for Nanoparticle Exposure Studies." *Journal of Nanoparticle Research* **11**(7):1611-1624.

Oberdorster G, Oberdorster E, Oberdorster J (2005). "Nanotoxicology: An Emerging Discipline Evolving from Studies of Ultrafine Particles." *Environmental Health Perspectives* **113**(7): 823-839.

Peters TM, Elzey S, Johnson R, Park H, Grassian VH, Maher T, O'Shaughnessy P (2009). "Airborne Monitoring to Distinguish Engineered Nanoparticles from Incidental Particles for Environmental Health and Safety." *Journal of Occupational and Environmental Hygiene* **6**(2): 73-81.

Photon Correlation Spectroscopy (PCS). (2006). Retrieved April 23, 2010, from http://www.beckmancoulter.com/coultercounter/homepage_tech_PCS.jsp

Rasband, W.S., ImageJ, U. S. National Institutes of Health, Bethesda, Maryland, USA, <http://rsb.info.nih.gov/ij/>, 1997-2009.

Schulte PA, Geraci CL, Schubauer-Berigan MK, Zumwalde R, Mayweather C, McKernan JL (2009). "Issues in the Development of Epidemiologic Studies of Workers Exposed to Engineered Nanoparticles." *JEOM* **51**(3): 323-335.

Thomas K, Aguar P, Kawasaki H, Morris J, Nakanishi J, Savage N (2006). "Research Strategies for Safety Evaluation of Nanomaterials, Part VIII: International Efforts to Develop Risk-Based Safety Evaluations for Nanomaterials." *Toxicological Sciences* **92**(1): 23-32.

Tsuji JS, Maynard AD, Howard PC, James JT, Lam C, Warheit DB, Santamaria AB (2006). "Research Strategies for Safety Evaluation of Nanomaterials, Part IV: Risk Assessment of Nanoparticles." *Toxicological Sciences* **89**(1): 42-50.

Weisner MR, Lowry GV, Jones KL, Hochella MF, Di Giulio RT, Casman E, Bernhardt ES (2009). "Decreasing Uncertainties in Assessing Environmental Exposure, Risk, and Ecological Implications of Nanomaterials." *Environmental Science and Technology* **43**: 6458-6462.

Appendix A – Particle Adhesion Calculations

Adhesive Forces: Calculations from Hinds (1999)

Largest particle diameter Smallest particle diameter

$$d_l := 240 \cdot \text{nm}$$

$$d_s := 15 \cdot \text{nm}$$

Average separation distance

$$x := 0.4 \cdot \text{nm}$$

Value for smooth surfaces

Hamaker Constant

$$\frac{A}{W} := 6 \cdot 10^{-20} \cdot \text{J}$$

The smallest value in the range provided by Hinds (1999) was used as a conservative estimate. A is material dependent.

For the largest particle size:

$$\Gamma_{\text{adh1}} := \frac{A \cdot d_l}{12 \cdot x^2} = 7.5 \times 10^{-9} \text{ N}$$

For the smallest particle size:

$$\Gamma_{\text{adh2}} := \frac{A \cdot d_s}{12 \cdot x^2} = 4.687 \times 10^{-10} \text{ N}$$

Compared to the force due to gravity:

For unit density particles

$$\rho := 1000 \frac{\text{kg}}{\text{m}^3}$$

Acceleration of gravity

$$g := 9.81 \frac{\text{m}}{\text{s}^2}$$

Mass of a large particle

$$V_l := \frac{\pi \cdot d_l^3}{6}$$

Mass of a small particle

$$V_s := \frac{\pi \cdot d_s^3}{6}$$

$$m_l := \rho \cdot V_l$$

$$m_s := \rho \cdot V_s$$

For the largest particle size:

$$F_{g1} := m_l \cdot g = 7.100703113867339 \cdot 10^{-17} \text{ N}$$

For the smallest particle size:

$$F_{g2} := m_s \cdot g = 1.7335700961590186 \cdot 10^{-20} \text{ N}$$

$$\frac{F_{\text{adh1}}}{F_{g1}} = 1.056 \times 10^8$$

$$\frac{F_{\text{adh2}}}{F_{g2}} = 2.704 \times 10^{10}$$

Appendix B – Thermophoretic Sampler Design Calculations (Equation Set 1)

Thermophoretic velocity and collection time calculations:

Given:

$$M := .029 \frac{\text{kg}}{\text{mol}} \quad \text{molecular weight of air}$$

$$m_{\text{air}} := \frac{M \cdot 1 \text{mol}}{6.02 \times 10^{23}} = 0 \text{kg} \quad \text{weight of an "air molecule" it's too small to be displayed. Done by calculator gives } 4.8\text{E-}26 \text{ kg}$$

$$k := 1.38 \cdot 10^{-23} \frac{\text{J}}{\text{K}} \quad \text{Boltzman's constant}$$

$$T_1 := 395 \text{K} \quad \text{Hot plate temp}$$

$$T_1 = 121.85^\circ\text{C}$$

$$T_2 := 285.2 \text{K} \quad \text{Cold plate temp}$$

$$T_2 = 12.05^\circ\text{C}$$

$$d_{\text{air}} := .0003710^{-6} \cdot \text{m} \quad \text{diameter of an "air molecule"}$$

$$\Delta T := \frac{385 \text{K} - 285.2 \text{K}}{.001 \text{m}}$$

$$\Delta T = 9.98 \times 10^4 \frac{\text{K}}{\text{m}} \quad \text{temperature gradient}$$

$$\eta_1 := \frac{2 \cdot \sqrt{m_{\text{air}} \cdot k \cdot T_1}}{3 \cdot \pi^{1.5} \cdot d_{\text{air}}^2}$$

$$\eta_1 = 1.417 \times 10^{-5} \text{Pa}\cdot\text{s} \quad \text{air viscosity at } 122 \text{ deg C}$$

$$\eta_2 := \frac{2 \cdot \sqrt{m_{\text{air}} \cdot k \cdot T_2}}{3 \cdot \pi^{1.5} \cdot d_{\text{air}}^2}$$

$$\eta_2 = 1.204 \times 10^{-5} \text{Pa}\cdot\text{s} \quad \text{air viscosity at } 12.2 \text{ deg C}$$

Thermophoretic velocity:

$$V_{th1} := \frac{.55 \cdot \eta_1 \cdot \Delta T}{1.2 \frac{\text{kg}}{\text{m}^3} \cdot T_1}$$

$$V_{th1} = 1.641 \times 10^{-3} \frac{\text{m}}{\text{s}} \quad \text{thermophoretic velocity at 122 deg C}$$

$$V_{th2} := \frac{.55 \cdot \eta_2 \cdot \Delta T}{1.2 \frac{\text{kg}}{\text{m}^3} \cdot T_2}$$

$$V_{th2} = 1.931 \times 10^{-3} \frac{\text{m}}{\text{s}} \quad \text{thermophoretic velocity at 12.2 deg C}$$

Horizontal velocity - 5 mL/min:

$$Q := 5 \frac{\text{cm}^3}{\text{min}} \quad \text{flow rate}$$

$$A := 1 \text{ mm} \cdot 5 \text{ mm} \quad \text{cross sectional area of flow chamber}$$

$$V := \frac{Q}{A}$$

$$V = 0.017 \frac{\text{m}}{\text{s}} \quad \text{air velocity through the flow chamber}$$

Collection time:

$$t_1 := \frac{1 \text{ mm}}{V_{th1}}$$

$$t_1 = 0.609 \text{ s} \quad \text{time to settle at 1st thermophoretic velocity}$$

$$t_2 := \frac{1 \text{ mm}}{V_{th2}}$$

$$t_2 = 0.518 \text{ s} \quad \text{time to settle at 2nd thermophoretic velocity}$$

Collection distance:

$$d_1 := t_1 \cdot V$$

$$d_1 = 10.15581 \cdot \text{mm} \quad \text{distance to collection for 122 deg C thermophoretic velocity}$$

$$d_2 := t_2 \cdot V$$

$$d_2 = 8.63 \cdot \text{mm} \quad \text{distance to collection for 12.2 deg C thermophoretic velocity}$$

Note: the distance to the end of the collection stub from edge of the cold plate is 11.3 mm

For these calculations to be valid, the flow through the collection chamber must be laminar ($Re < 2000$ for flow through ducts). The following calculations check the Reynolds numbers to verify this:

density of air

$$\rho := 1.2 \frac{\text{kg}}{\text{m}^3}$$

Characteristic dimension (largest used to get a conservative estimate)

$$d := 5 \cdot \text{mm}$$

$$Re_{\eta_1} := \frac{\rho \cdot V \cdot d}{\eta_1} = 7.056$$

For air viscosity at hot plate temperature

$$Re_{\eta_2} := \frac{\rho \cdot V \cdot d}{\eta_2} = 8.304$$

For air viscosity at cold plate temperature

Horizontal velocity - 20 mL/min:

$$\dot{Q} := 20 \frac{\text{cm}^3}{\text{min}} \quad \text{flow rate}$$

$$\dot{A} := 1\text{mm} \cdot 5\text{mm} \quad \text{cross sectional area of flow chamber}$$

$$\dot{V} := \frac{Q}{A}$$

$$V = 0.067 \frac{\text{m}}{\text{s}} \quad \text{air velocity through the flow chamber}$$

Collection time:

$$t_{th1} := \frac{1\text{mm}}{V_{th1}}$$

$$t_1 = 0.609 \text{ s} \quad \text{time to settle at 1st thermophoretic velocity}$$

$$t_{th2} := \frac{1\text{mm}}{V_{th2}}$$

$$t_2 = 0.518 \text{ s} \quad \text{time to settle at 2nd thermophoretic velocity}$$

Collection distance:

$$d_{1V} := t_1 \cdot V$$

$$d_1 = 40.62324 \cdot \text{mm} \quad \text{distance to collection for 122 deg C thermophoretic velocity}$$

$$d_{2V} := t_2 \cdot V$$

$$d_2 = 34.518 \cdot \text{mm} \quad \text{distance to collection for 12.2 deg C thermophoretic velocity}$$

Note: the distance to the end of the collection stub from edge of the cold plate is 11.3 mm

For these calculations to be valid, the flow through the collection chamber must be laminar ($Re < 2000$ for flow through ducts). The following calculations check the Reynolds numbers to verify this:

density of air

$$\rho := 1.2 \frac{\text{kg}}{\text{m}^3}$$

Characteristic dimension (largest used to get a conservative estimate)

$$d := 5 \cdot \text{mm}$$

$$Re_{\eta_1} := \frac{\rho \cdot V \cdot d}{\eta_1} = 28.225$$

For air viscosity at hot plate temperature

$$Re_{\eta_2} := \frac{\rho \cdot V \cdot d}{\eta_2} = 33.217$$

For air viscosity at cold plate temperature

Appendix C – Thermophoretic Sampler Design Calculations (Equation Set 2)

Thermophoretic Velocities

For Particles with diameter much smaller than air mean free path
(about .066 micrometers).

$$\eta := 184.6 \cdot 10^{-7} \frac{\text{N} \cdot \text{s}}{\text{m}^2} \quad \text{Air viscosity}$$

$$\rho := 1.1614 \frac{\text{kg}}{\text{m}^3} \quad \text{Density of air}$$

$$T_1 := 285.35\text{K} \quad \text{Temperature of the cold plate}$$

$$T_2 := 395.15\text{K} \quad \text{Temperature of the hot plate}$$

$$\text{DelT} := \frac{T_2 - T_1}{1\text{mm}} \quad \text{Temperature gradient}$$

$$\lambda := 0.066 \cdot 10^{-6} \quad \text{Mean free path of air}$$

$$k_a := 0.0263 \frac{\text{W}}{\text{m} \cdot \text{K}} \quad \text{Thermal conductivity of air}$$

$$k_p := 66.9 \frac{\text{W}}{\text{m} \cdot \text{K}} \quad \text{Thermal conductivity of the particles}$$

For particles larger than say 100 nm use correction factors and inner temperature gradient

$d_p := (.01 \cdot 10^{-6}, .02 \cdot 10^{-6} \dots 3 \cdot 10^{-6})$ For a range of particles from 10 nm to 300 nm

$$H(d_p) := \left(\frac{1}{1 + \frac{6 \cdot \lambda}{d_p}} \right) \cdot \left[\frac{\frac{k_a}{k_p} + 4.4 \cdot \left(\frac{\lambda}{d_p} \right)}{1 + 2 \cdot \left(\frac{k_a}{k_p} \right) + 8.8 \cdot \left(\frac{\lambda}{d_p} \right)} \right]$$

	$H(d_p) =$
20 nm	0.012
	0.023
	0.033
50 nm	0.043
	0.052
	0.06
	0.067
	0.074
100 nm	0.08
	0.086
	0.091
	0.096
	0.101
	0.105
	0.109
	0.113
	0.116
	0.119
240 nm	0.122
	0.125
	0.127
	0.13
	0.132
	0.134
	0.135
	0.137
	0.138
	0.14
0.141	
	0.142

Cunningham correction factor

$$C_c(d_p) := 1 + \frac{\lambda}{d_p} \cdot \left[2.34 + 1.05 \cdot e^{-.039 \cdot \left(\frac{d_p}{\lambda} \right)} \right]$$

	$C_c(d_p) =$
	23.333
	12.146
20 nm	8.417
	6.553
	5.434
50 nm	4.689
	4.156
	3.757
	3.446
	3.198
100 nm	2.994
	2.825
	2.682
	2.559
	2.452
	2.359
	2.277
	2.204
	2.139
	2.08
	2.027
	1.979
	1.934
	1.894
240 nm	1.857
	1.823
	1.791
	1.761
	1.734
	1.708

Thermophoretic velocity

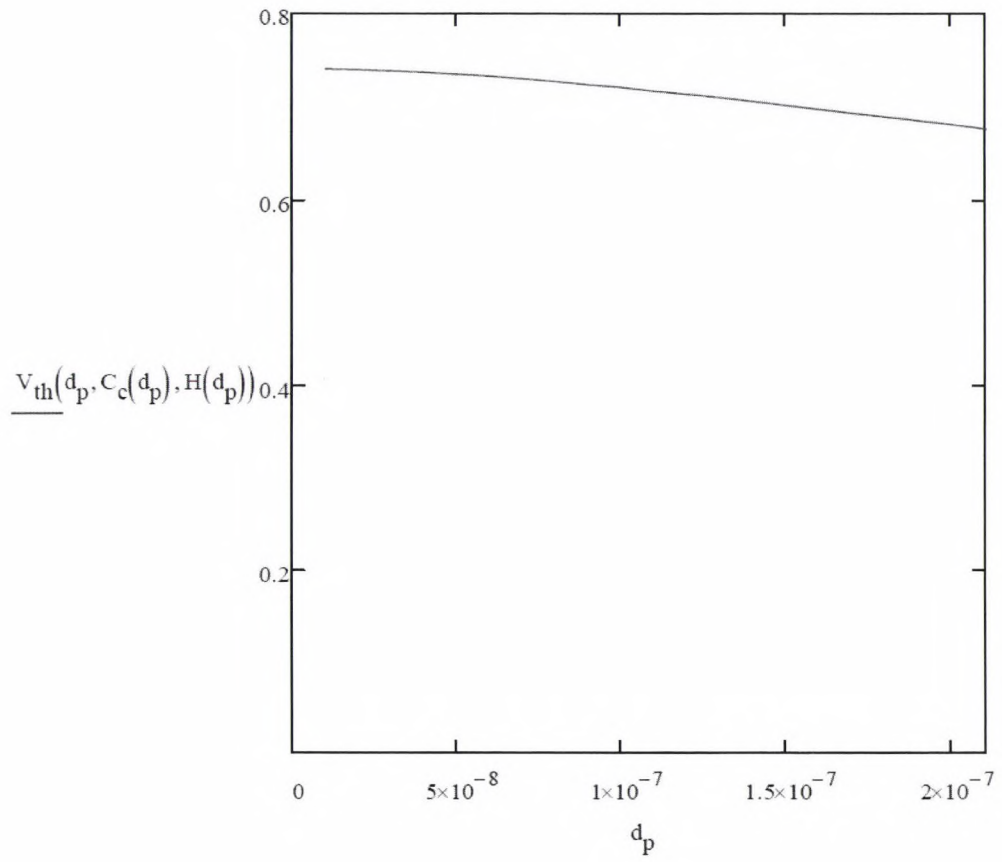
$$V_{th}(d_p, H, C_c) := \frac{3 \cdot C_c \cdot H \cdot \eta \cdot \Delta T}{2 \cdot \rho \cdot T}$$

Percent change in V_{th} due to temperature gradients in the particles

$$\frac{2.465 - 2.207}{2.465} \cdot 100 = 10.467$$

	$V_{th}(d_p, C_c(d_p), H(d_p)) =$	$\frac{A \cdot m \cdot K \cdot s}{kg}$
20 nm	0.74	
	0.739	kg
	0.738	
50 nm	0.736	
	0.734	
	0.732	
	0.729	
	0.726	
100 nm	0.723	
	0.72	
	0.716	
	0.713	
	0.709	
	0.705	
	0.701	
240 nm	0.697	
	0.693	
	0.688	
	0.684	
	0.68	
	0.675	
	0.671	
	0.666	
	0.662	
	0.658	
	0.653	
0.649		
0.644		
0.64		
0.636		

Particle diameter vs. thermophoretic velocity



Time to go from top plate to bottom plate

$$\text{Time}(d_p, C_c, H, V_{th}) := \frac{.001}{V_{th}(d_p, C_c, H)} \text{m}$$

	$\text{Time}(d_p, C_c(d_p), H(d_p), V_{th}) =$	
20 nm	$1.352 \cdot 10^{-3}$	$\frac{\text{kg}}{\text{A} \cdot \text{K} \cdot \text{s}}$
	$1.353 \cdot 10^{-3}$	
	$1.355 \cdot 10^{-3}$	
50 nm	$1.358 \cdot 10^{-3}$	
	$1.362 \cdot 10^{-3}$	
	$1.366 \cdot 10^{-3}$	
	$1.371 \cdot 10^{-3}$	
	$1.377 \cdot 10^{-3}$	
100 nm	$1.383 \cdot 10^{-3}$	
	$1.389 \cdot 10^{-3}$	
	$1.396 \cdot 10^{-3}$	
	$1.403 \cdot 10^{-3}$	
	$1.411 \cdot 10^{-3}$	
	$1.419 \cdot 10^{-3}$	
	$1.427 \cdot 10^{-3}$	
	$1.435 \cdot 10^{-3}$	
	$1.444 \cdot 10^{-3}$	
	$1.453 \cdot 10^{-3}$	
	$1.462 \cdot 10^{-3}$	
240 nm	$1.471 \cdot 10^{-3}$	
	$1.481 \cdot 10^{-3}$	
	$1.491 \cdot 10^{-3}$	
	$1.5 \cdot 10^{-3}$	
	$1.51 \cdot 10^{-3}$	
	$1.521 \cdot 10^{-3}$	
	$1.531 \cdot 10^{-3}$	
	$1.541 \cdot 10^{-3}$	
	$1.552 \cdot 10^{-3}$	
	$1.563 \cdot 10^{-3}$	
	$1.573 \cdot 10^{-3}$	

Residence Time - 5 mL/min

$$Q := 5 \frac{\text{cm}^3}{\text{min}} \quad L_{XS} := 5\text{mm} \quad H_{XS} := 1\text{mm} \quad L := 12\text{mm} \quad A_{XS} := L_{XS} \cdot H_{XS}$$

$$\text{Vol} := L_{XS} \cdot H_{XS} \cdot L \quad \text{Vol} = 0.06 \cdot \text{cm}^3$$

$$\text{Vel}_{\text{horiz}} := \frac{Q}{A_{XS}} \quad \text{Vel}_{\text{horiz}} = 1.667 \cdot \frac{\text{cm}}{\text{s}}$$

Calculation of collection zone

For largest particle V.th is 2.2 mm/s and residence time is 0.45 s.

$$\text{Vel}_{\text{horiz}} = 0.017 \frac{\text{m}}{\text{s}} \quad T_{\text{res1}} := 0.453\text{s} \quad \text{Dist}_{\text{coll1}} := \text{Vel}_{\text{horiz}} \cdot T_{\text{res1}}$$

$$\text{Dist}_{\text{coll1}} = 7.55 \cdot \text{mm}$$

For smallest particle V.th is 2.47 mm/s and residence time is 0.406 s.

$$\text{Vel}_{\text{horiz}} = 0.017 \frac{\text{m}}{\text{s}} \quad T_{\text{res2}} := 0.406\text{s} \quad \text{Dist}_{\text{coll2}} := \text{Vel}_{\text{horiz}} \cdot T_{\text{res2}}$$

$$\text{Dist}_{\text{coll2}} = 6.767 \cdot \text{mm}$$

Checking that flow is laminar:

Characteristic dimension

$$d := 5 \cdot \text{mm}$$

Using larger value for a conservative estimate

Velocity through the device

$$\text{Vel}_{\text{horiz}} = 0.017 \frac{\text{m}}{\text{s}}$$

$$\text{Re} := \frac{\rho \cdot d \cdot \text{Vel}_{\text{horiz}}}{\eta} = 5.243$$

Residence Time - 20 mL/min

$$Q := 20 \frac{\text{cm}^3}{\text{min}} \quad L_{\text{XS}} := 5 \text{ mm} \quad H_{\text{XS}} := 1 \text{ mm} \quad L := 12 \text{ mm} \quad A_{\text{XS}} := L_{\text{XS}} \cdot H_{\text{XS}}$$

$$Vol := L_{\text{XS}} \cdot H_{\text{XS}} \cdot L \quad Vol = 0.06 \cdot \text{cm}^3$$

$$Vel_{\text{horiz}} := \frac{Q}{A_{\text{XS}}} \quad Vel_{\text{horiz}} = 6.667 \cdot \frac{\text{cm}}{\text{s}}$$

Calculation of collection zone

For largest particle V.th is 2.2 mm/s and residence time is 0.45 s.

$$Vel_{\text{horiz}} = 0.067 \frac{\text{m}}{\text{s}} \quad T_{\text{res1}} := 0.453 \text{ s} \quad Dist_{\text{coll1}} := Vel_{\text{horiz}} \cdot T_{\text{res1}}$$

$$Dist_{\text{coll1}} = 30.2 \cdot \text{mm}$$

For smallest particle V.th is 2.47 mm/s and residence time is 0.406 s.

$$Vel_{\text{horiz}} = 0.067 \frac{\text{m}}{\text{s}} \quad T_{\text{res2}} := 0.406 \text{ s} \quad Dist_{\text{coll2}} := Vel_{\text{horiz}} \cdot T_{\text{res2}}$$

$$Dist_{\text{coll2}} = 27.067 \cdot \text{mm}$$

Checking that flow is laminar:

Characteristic dimension

$$d := 5 \cdot \text{mm}$$

Using larger value for a conservative estimate

Velocity through the device

$$Vel_{\text{horiz}} = 0.067 \frac{\text{m}}{\text{s}}$$

$$Re := \frac{\rho \cdot d \cdot Vel_{\text{horiz}}}{\eta} = 20.971$$

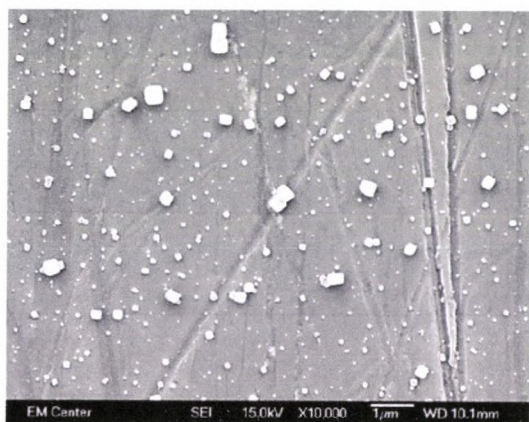
Appendix D – ImageJ Particle Counting Procedure

This procedure is based off of the “Particle Counting and Analysis” tutorial from the ImageJ website: <http://rsbweb.nih.gov/ij/docs/pdfs/examples.pdf>

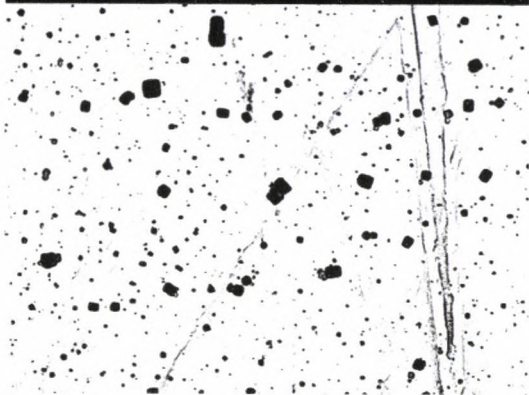
After opening the image in ImageJ:

1. Set Global Scale
 - a. Using the line tool from the tool bar, draw a line on the scale bar.
 - b. Select **Analyze**→**Set Scale**.
 - c. In the “Known Distance” text area, type 1000.
 - d. Change “Unit of Length” to nm (default is inch).
 - e. Check the “Global” box.
 - f. Press “OK.”
2. Change to Gray Scale
 - a. **Image**→**Type**→**8-Bit**
3. Adjust Brightness and Contrast
 - a. **Image**→**Adjust**→**Brightness/Contrast**.
 - b. Using “Minimum” and “Maximum” sliders, maximize the contrast between the particles and the background.
 - c. Click “Apply.”
 - d. Close the Brightness/Contrast window.
4. Change to Binary
 - a. **Process**→**Binary**→**Make Binary**.
5. Analyze Particles
 - a. Erase scale bar.
 - i. Using the box tool from the tool bar, draw a box around the scale bar.
 - ii. **Edit**→**Clear**.
 - b. **Analyze**→**Analyze Particles**.
 - c. Enter range of particle areas to be counted (e.g. 41-65 nm \approx 5001-13250 nm²).
 - d. Enter 0.3-1.00 as the range for “Circularity”.
 - e. **Show**→**Outlines**.
 - f. Check “Display Results” box.
 - g. Click “OK.”
 - h. Verify accurate counting by comparing original image to outlines.
 - i. Record results.

An example series of images is presented in Figure D.1.



A.



B.



C.

Figure D.1. A) Original image. B) Binary image. C) Outlines for counts (41-65 nm).